The simulation of femtosecond VUV time-resolved molecular spectroscopy

Michael Robert Coates

A thesis presented for the degree of

Master of Science

uOttawa

Department of Chemistry and Biomolecular Sciences

University of Ottawa

The simulation of femtosecond VUV time-resolved molecular spectroscopy

Michael Robert Coates

Abstract

Femtosecond vacuum-ultraviolet (VUV) laser pulses enable the interrogation of molecules in their electronically excited states on the timescale of nuclear motion. The present study focuses on the simulation of these experiments using electronic structure calculations and nuclear wavepacket dynamics propagations. The simulation of the evolution of the wavepacket enables a calculation of spectroscopic observables using rigorous quantum mechanical approaches. This approach has been applied to simulate the VUV time-resolved photoelectron spectroscopy (TRPES) spectra of cyclopropane (C_3H_6) and nitromethane (CH_3NO_2).

Declaration

I declare that all theoretical work summarized in the following chapters is work completed solely by myself with guidance from Dr. Michael Schuurman and Dr. Simon Neville.

Acknowledgements

I want to thank all of the members of the group that I have been a part of for the last few years. Dr. Simon Neville, you have been a great source of guidance on numerous projects without whom they would not have been completed. Dr. Issaka Seidu, it has been a pleasure sharing our desk space and hearing your laugh. Ryan MacDonell, I spelled your name correctly and you deserve a lot of praise for getting me started at this gig in the first place! Finally, I would like to acknowledge Dr. Michael Schuurman for advising me over the last few years. I feel that I have learned more in two years in your group than I have in a decade.

Contents

List of Figures

List of Tables

List of Publications

Coates, M. R.; Larsen, M. A. B.; Forbes, R.; Neville, S. P.; Boguslavskiy, A. E.; Wilkinson, I.; Sølling, T. I.; Lausten, R.; Stolow, A.; Schuurman, M. S. "*Vacuum ultraviolet excited state dynamics of the smallest ring, cyclopropane. II. Time-resolved photoelectron spectroscopy and ab initio dynamics.*" J. Chem. Phys., **2018**, *149* (14), 144311.

Chapter 1

Introduction

1.1 Motivation

The absorption of light by a molecule causes structural and electronic changes that promote chemical processes such as isomerization and bond breaking. The ability to discern the dynamics that immediately follow the absorption of light requires the interrogation of molecule on the inherent vibrational timescales. For example, photochemical bond breaking and bond formation can occur on a femtosecond (10^{-15} s) timescale, where few vibrational periods occur before the photochemical processes has completed. Accordingly, femtosecond laser pulses are required to study molecules in their electronically excited states on a timescale sensitive to their motion.

The objective of studying ultrafast excited state processes in a time-resolved fashion is to discern the coupled electronic-vibrational dynamics (i.e. mechanisms) that underlie photochemical reactions. Time-independent experimental techniques can accurately determine branching ratios but cannot elucidate the vibronic mechanisms that lead to the outcome of a reaction. In these experiments the reactants and products of a reaction can be characterized, however, a mechanism must be inferred. The use of femtosecond light pulses allows for the study of a molecular wavepacket that can be probed as a function of time, yielding a spectral signal that corresponds to dynamics occurring on the excited state. If the photon energy of the laser pulse involves ultraviolet radiation, this will generally correspond to the energy separation between electronic states in organic molecules. Furthermore, since excited states will exist within a manifold, the ensuing molecular dynamics will generally involve multiple electronic states. Time-dependent experimental signals are complex and involve

the coupling of vibrational and electronic degrees of freedom and thus the resulting experimental observable is difficult to interpret without theoretical modelling and simulation.

The present work concerns the study of photoinduced processes and the reaction mechanisms that lead to their decay. In order to study these reaction mechanisms, we employ *ab initio* simulations informed by multi-reference electronic structure theory to calculate. The results are coupled with time-resolved photoelectron spectroscopy (TRPES) measurements in order to understand the molecular dynamics occurring on the excited state. The first chapter pertains to the relevant theory that is necessary to describe the calculations contained in the subsequent chapters. The second chapter pertains to the photodissociation of the smallest ring, cyclopropane (C_3H_6). The third chapter pertains to the photodissociation and photoisomerization of the smallest nitro-substituted hydrocarbon, nitromethane (CH_3NO_2).

1.2 Theory

1.2.1 The Schrödinger Equation

In a molecular system, the electronic and nuclear degrees of freedom are described by the full molecular Hamiltonian acting on a wavefunction via the Schrödinger equation:

$$\hat{H}\Psi(\mathbf{r},\mathbf{R}) = E\Psi(\mathbf{r},\mathbf{R}) \tag{1.1}$$

where $\mathbf{r}$ are the electronic coordinates, $\mathbf{R}$ are the nuclear coordinates and $\hat{H}$ corresponds to the full molecular Hamiltonian that describes the interactions of the particles in the system. The Schrödinger equation is an eigenvalue equation that returns an energy E following the operation of the molecular Hamiltonian on the total molecular wavefunction, $\Psi(\mathbf{r},\mathbf{R})$. The molecular Hamiltonian takes the form:

$$\hat{H} = \hat{T}_N + \hat{T}_e + \hat{U}_{eN} + \hat{U}_{ee} + \hat{U}_{NN} \tag{1.2}$$

where the kinetic energy of the nuclei $\hat{T}_N$ and electrons $\hat{T}_e$ and the Coulombic attraction of the nuclei and electrons $\hat{U}_{eN}$, the electron-electron $\hat{U}_{ee}$ and nuclear-nuclear $\hat{U}_{NN}$ repulsion are described. The wavefunction *ansatz* is taken as a product of nuclear and electronic wavefunctions via the Born-Huang expansion[1]:

$$\Psi(\mathbf{r},\mathbf{R}) = \sum_i \psi_i(\mathbf{r};\mathbf{R})\chi_i(\mathbf{R}) \tag{1.3}$$

The electronic wavefunctions are not arbitrary and are in fact eigenfunctions of the electronic Schrödinger equation:

$$\hat{H}_e\psi_j(\mathbf{r};\mathbf{R}) = E_j(\mathbf{R})\psi_j(\mathbf{r};\mathbf{R}) \tag{1.4}$$

where $\hat{H}_e$ is the electronic Hamiltonian takes the form:

$$\hat{H}_e = \hat{T}_e + \hat{U}_{eN} + \hat{U}_{ee} + \hat{U}_{NN}. \tag{1.5}$$

Here the nuclear kinetic operator $\hat{T}_N$ is excluded, meaning that the electronic motion is uncoupled from the nuclear motion but parametrically depends on the nuclear coordinates. The insertion of the total wavefunction into the Schrödinger equation, followed by multiplication by $\psi_j^*(\mathbf{r};\mathbf{R})$ and integration over the electronic coordinates leads to the following equation for the nuclear wavefunctions:

$$\boxed{[E_j(\mathbf{R}) + \hat{T}_N]\chi_i(\mathbf{R}) - \sum_i \Lambda_{ji}\chi_i(\mathbf{R}) = E\chi_j(\mathbf{R})} \tag{1.6}$$

Here the $E_j(\mathbf{R})$ are the electronic potential energy surfaces that arise from the operation of the electronic Hamiltonian acting on the wavefunction. Additionally, the Λ_{ji} are the *non-adiabatic* coupling terms that couple the electronic and nuclear degrees of freedom. These terms take the form,

$$\Lambda_{ji} = \frac{1}{2\mathbf{M}}[2\mathbf{F}_{ji}\cdot\nabla + G_{ji}] \tag{1.7}$$

where $\mathbf{M}$ is the nuclear mass, and $\mathbf{F}_{ji}$ and G_{ji} are the *derivative* and *scalar* couplings, respectively. The setting of the *non-adiabatic* coupling terms to zero results in the Born-Oppenheimer approximation (BOA)[2], where the electronic and nuclear degrees of freedom are completely un-coupled. The exclusion of these terms gives rise to the concept of nuclear wavefunctions evolving on single potential energy surfaces, $E_j(\mathbf{R})$. In regions where the difference between potential energy surfaces is small, the coupling terms Λ_{ji} become large and the BOA breaks down. In the description of electronically excited states, often the coupling of nuclear and electronic degrees of freedom is necessary and therefore the coupling terms must be included.

1.3 Electronic Structure Theory

1.3.1 Hartree-Fock Theory and the Self-Consistent Field Method

The Pauli exclusion principle[3] states that two electrons cannot occupy the same quantum state i.e. the same space and spin and the exchange of any two electrons should result in the change of sign of the wavefunction. To address this, the electronic wavefunction can be represented as a linear combination of Hartree products (a wavefunction taken as a product of one-electron functions) via a Slater determinant:

$$\Phi = \frac{1}{\sqrt{N}} \begin{vmatrix} \phi_i(\mathbf{x}_1) & \dots & \phi_k(\mathbf{x}_1) \\ \vdots & \ddots & \vdots \\ \phi_i(\mathbf{x}_N) & \dots & \phi_k(\mathbf{x}_N) \end{vmatrix} \tag{1.8}$$

Here, the rows denote the electrons and the columns denote the orbitals and where $\mathbf{x}_i = \{\mathrm{r}_i, \omega\}$ are the electronic coordinates (r_i) with an associated spin function (ω). The representation of the wavefunction as a single Slater determinant is convenient for addressing the requirement that the wavefunction should be anti-symmetric with respect to the exchange of any two electrons, because the sign of a determinant changes if any two columns are exchanged.

A convenient starting point for the description of electronic structure is with the Hartree-Fock (HF) method[4], which takes the electronic wavefunction as a single Slater determinant. The optimization of the spin-orbital energies follows a the variational theorem which gives the optimized energies that are an upper bound to the exact energy. This follows a *self-consisten field* (SCF) method[5], whereby the solutions of the optimization depend on the orbitals and thus a trial wavefunction is required. The HF equations consist of an eigenvalue problem,

$$f(\mathbf{x}_a)\phi_i(\mathbf{x}_a) = \epsilon_i\phi_i(\mathbf{x}_a) \tag{1.9}$$

where the equations are simply the algebraic solution to the insertion of the single Slater determinant into the electronic Schrödinger equation. Here, $f(\mathbf{x}_a)$ is the the Fock operator acting on the i^{th} spin-orbital and where where ϵ_i is the associated orbital energy. The Fock operator,

$$f(\mathbf{x}_a) = h(\mathbf{x}_a) + \sum_i \mathcal{J}_i(\mathbf{x}_a) - \mathcal{K}_i(\mathbf{x}_a) \tag{1.10}$$

consists of the core-Hamiltonian $h(\mathbf{x}_a)$, Coulomb $\mathcal{J}_i(\mathbf{x}_a)$ and exchange $\mathcal{K}_i(\mathbf{x}_a)$ operators. The core-Hamiltonian,

$$h(\mathbf{x}_a) = -\frac{1}{2}\nabla_a^2 + \sum_A \frac{Z_A}{r_{aA}} \tag{1.11}$$

is taken as a sum of the kinetic energy of the a^{th} electron and the interaction of the a^{th} electron with the A^{th} nucleus. The Coulomb and exchange operators are defined as

$$\mathcal{J}_i(\mathbf{x}_a) = \langle \phi_i(\mathbf{x}_b)| \, r_{ab}^{-1} \, |\phi_i(\mathbf{x}_b)\rangle \tag{1.12}$$

and

$$\mathcal{K}_i(\mathbf{x}_a)\phi_j(\mathbf{x}_a) = \langle \phi_i(\mathbf{x}_b)| \, r_{ab}^{-1} \, |\phi_i(\mathbf{x}_b)\rangle \, \phi_j(\mathbf{x}_a) \tag{1.13}$$

The Coulomb operator ($\mathcal{J}_i(\mathbf{x}_a)$) accounts for the interaction of an electron with an average potential given by all other electrons. The exchange operator ($\mathcal{K}_i(\mathbf{x}_a)$) has no classical analogue and is the result of the wavefunction ansatz. The HF wavefunction provides a good zeroth-order description of the ground state potential energy surface, particularly in the region of equilibrium geometry of a molecule. In systems involving large amplitude motion such as bond-breaking or bond-formation, the HF wavefunction fails to describe the potential energy surfaces, where the description of open-shell (unpaired electron) molecules is not described by a single Slater determinant. Additionally, HF can describe the correlation of same spin electrons, however, it can not account for correlations between opposite spin electrons. This lack of *electron correlation* leads to an error in the HF energy.

1.3.2 Electron Correlation

The difference between the HF energy E_{HF} and the exact energy E_{Exact} is called electron correlation energy:

$$E_{corr} = E_{\text{Exact}} - E_{\text{HF}} \tag{1.14}$$

Electron correlation is comprised of exchange, dynamic and static correlation. The HF wavefunction accounts for exchange correlation via the Pauli exclusion principle, where the probability of occupying same point in space is zero. It does not account for dynamic correlation which arises due to the instantaneous Coulombic repulsion of electrons of opposite spin. To address this, the HF wavefunction can be expanded as a sum of N-tuple excitations from the HF reference space in a method called *configuration interaction* (CI):

$$|\psi\rangle = c_0 |\Phi_0\rangle + \sum_{ia} c_i^a |\Phi_i^a\rangle + \sum_{i<j,a<b} c_{ij}^{ab} |\Phi_{ij}^{ab}\rangle + \sum_{i<j<k,a<b<c} c_{ij}^{ab} |\Phi_{ijk}^{abc}\rangle + \dots \quad (1.15)$$

Here, the upper bound to the summation is the total number of occupied electrons. Including all possible excitations, a numerically exact result is obtained by doing full configuration interaction (FCI). The expansion of the reference determinant into a sum of N-tuply excited determinants scales factorially with the number of electrons and orbitals in a molecule and is computationally intractable. By truncating the full expansion to single (CIS) or double (CISD) excitations, this provides the wavefunction with a degree of dynamic correlation that correlates electrons of opposite spins, while being computationally feasible.

1.3.3 Multireference Electronic Structure

The last type of electron correlation is static correlation which arises from the necessity to include nearly degenerate determinants in the description of the wavefunction. This is particularly important in cases where the zeroeth order approximation that the wavefunction can be represented by a single Slater determinant breaks down, specifically in the description of the formation and breaking of bonds. Here, at least two references are required to describe the two fragments of a molecule following the formation and cleavage of a bond, respectively. In the most simple case of the homolytic bond breaking of H_2, the HF wavefunction fails to describe the correct dissociation energy. This is because the bonding and anti-bonding orbitals become degenerate and a single electronic configuration fails to provide a reasonable description of both fragments. A method of generating multiple determinants is through the selection of an orbital subspace, called an active space, where full configuration interaction is performed. The process by which the wavefunction is optimized is

through the complete active-space self-consistent field (CASSCF) method[6] which has the wavefunction ansatz:

$$\left|\psi^{CASSCF}\right\rangle = \sum_{I} C_I \left|\Phi_I\right\rangle \tag{1.16}$$

where C_I are the coefficients multiplying the Slater determinants, Φ_I. The CASSCF procedure simultaneously optimizes the orbital energies and the coefficients on each determinant subject to the averaging over a select number of electronic states. By including additional orbital subspaces, the restricted active-space self-consistent field (RASSCF) method[7] can be defined. Here the CASSCF orbital subspace is denoted RAS2, while additional occupied and virutal orbital subspaces are denoted RAS1 and RAS3, respectively. Excitations are performed out of RAS1 into RAS2 and RAS3, while excitations are also performed out of RAS2 into RAS3. While N-electron excitations can be considered in RAS2, excitations involving RAS1 and RAS3 are truncated to low order (i.e. $N_{exc} = 1, 2, 3$). These additional orbital subspaces allow for additional configurations to be generated, while also including additional orbitals in the description of the wavefunction. Using the CASSCF/RASSCF wavefunction as as a starting guess to perform all possible single excitations from results in a first-order multi-reference CI wavefunction:

$$\left|\psi^{MRCI}\right\rangle = \sum_{I} C_I \left|\Phi_I\right\rangle + \sum_{I} \sum_{a,r} \hat{E}_a^r \left|\Phi_I\right\rangle \tag{1.17}$$

Here $\hat{E}_a^r$ is an operator which singly excites electrons in each determinant taken from the CASSCF/RASSCF reference wavefunction. The result is a wavefunction that can provide an excellent description of bond-breaking in electronically excited molecules. In general, the simulation of excited state dynamics occurring on multiple electronic states will require multi-reference electronic structure methods that account for static and dynamic correlation.

1.4 Quantum Dynamics

Excited state dynamics are characterized by potential energy surfaces that are complex and involve strong nonadiabatic coupling. This is the case at points of strong nonadiabatic coupling between excited states, called *conical intersections*, which mediate the localized transfer of population between excited states.

The treatment of the nuclear and electronic degrees of freedom by a method of simulation can either be fully quantum mechanical or a mixed quantum/classical. Mixed quantum/classical methods such as fewest-switches surface hopping (FSSH)[8] or Ehrenfest trajectory dynamics[9] treat the nuclear degrees of freedom classically. In FSSH, the classical trajectories stochastically hop from one electronic excited state to another by satisfying the conditions of a hopping probability that is determined from an electronic structure calculation[10]. In Ehrenfest dynamics, the equations of motion are entirely classical, where the trajectories evolved on an average of all electronic states with the forces on the nuclei being calculated from an electronic wavefunction or density matrix[11, 12]. The mixed quantum/classical methods have known pathological problems that make them less ideal for the description of excited state dynamics. In FSSH an individual trajectory propagates independently from all other trajectories and therefore a large number of trajectories are needed for statistical convergence. FSSH also suffers from de-coherence problems whereby the trajectories on different states are not able to separate. In Ehrenfest dynamics, the average potentials provide a poor description of the dynamics when surfaces that diverge, which does not allow the wavepacket to bifurcate. In both cases, the result is un-physical branching ratios in photochemical reactions and incorrect timescales for decay.

A quantum mechanical treatment of both the nuclear and electronic degrees of freedom is challenging. The treatment of the nuclear degrees of freedom can be done by expanding the nuclear wavefunction as a sum of *frozen* (fixed width) Gaussian basis functions[13, 14]. The *variational* multiconfigurational Gaussian (vMCG) method treats the nuclear wavefunction as a sum of *frozen* Gaussain basis functions, treating all parameters fully quantum mechanically. The equations-of-motion in vMCG are determined variationally by solving the *time*-dependent Schrödinger equation, however, issues in vMCG arise from the integration of the equations of motion and the presence of singularities in the equations of motion.

The *ab initio* multiple spawning (AIMS) method[15–17] makes use of an adaptive set of basis functions that are subject to increase as the nuclear wavefunction is evolved. The Gaussian basis functions follow the classical equations of motion with *time*-dependent coefficients multiplying the individual basis functions. At each time-step, the simultaneous solution of the nuclear Schrödinger equation is solved to evolve the coefficients multiplying the basis functions. The quantities required to solve the equations of motion are calculated *on-the-fly* as the nuclear trajectories

are propagated forward in time. The principle of the adaptive basis is akin to FSSH, but rather than stochastically hopping from one electronic state to another, the basis functions *spawn* basis functions on the other electronic states with an associated position, momentum and amplitude that is determined from an overlap with the parent basis function. The result is that AIMS can provide an accurate description of lifetimes and branching ratios as the nuclear wavefunction evolves on the electronically excited state potential energy surfaces.

1.4.1 *Ab initio* multiple spawning

In the framework of the total nuclear wavefunction expansion and the BOA, the solution of the potential energy surfaces (E_j) is computed via electronic structure methods. The nuclear basis functions are evaluated via classical equations of motion where the forces on the nuclei are taken from the gradients computed by electronic structure theory. The *ab initio* multiple spawning (AIMS) wavefunction ansatz takes the following form:

$$\chi_I(\mathbf{R}, t) = \sum_{j=1}^{N_I(t)} c_j^I(t)\chi_j^I(\mathbf{R}; \bar{R}_j^I(t), \bar{P}_j^I(t), \gamma_j^I(t), \alpha_j^I) \tag{1.18}$$

Here, the nuclear wavefunction for each electronic state is taken as a sum of multi-dimensional frozen Gaussian basis functions with time-dependent coefficients ($c_j^I(t)$). The individual nuclear basis functions are taken as a product of one-dimensional Gaussian basis functions:

$$\chi_j^I(\mathbf{R}; \bar{R}_j^I(t), \bar{P}_j^I(t), \gamma_j^I(t), \alpha_j^I) = e^{i\gamma_j^I(t)t} \prod_{\rho=1}^{3N} \chi_{\rho_j}^I(R; \bar{R}_{\rho_j}^I, \bar{P}_{\rho_j}^I, \alpha_{\rho_j}^I) \tag{1.19}$$

$$\chi_{\rho_j}^I(R_{\rho_j}; \bar{R}_{\rho_j}^I, \bar{P}_{\rho_j}^I, \alpha_{\rho_j}^I) = \left(\frac{2\alpha_{\rho_j}^I}{\pi}\right)^{\frac{1}{4}} \prod_{\rho=1}^{3N} exp[-\alpha_{\rho_j}^I(R_{\rho_j} - \bar{R}_{\rho_j}^I(t))^2 \tag{1.20}$$

$$+ i\bar{P}_{\rho_j}^I(t)(R_{\rho_j} - \bar{R}_{\rho_j}^I(t))] \tag{1.21}$$

Here the indices j indicate the nuclear basis function, while the superscript I indicates the electronic state that the basis functions is propagating in. The time-dependent total number of basis functions denoted by $N_I(t)$, is indicative of the spawning of new basis functions and is subject to change as the nuclear trajectory

is generated. Each basis function is paramaterized with a time-independent width ($\alpha^I_{\rho_j}$) and a time-dependent position $\bar{R}^I_{\rho_j}(t)$, momentum $\bar{R}^I_{\rho_j}(t)$ and phase $\gamma^I_j(t)$. The evolution of each Gaussian basis function is governed by classical equations-of-motion:

$$\frac{\partial \bar{R}^I_{\rho_j}(t)}{\partial t} = \frac{\bar{P}^I_{\rho_j}(t)}{m_\rho} \tag{1.22}$$

$$\frac{\partial \bar{P}^I_{\rho_j}(t)}{\partial t} = -\frac{V_I(\mathbf{R})}{\partial R_{\rho_j}}\bigg|_{\bar{R}^I_{\rho_j}(t)} \tag{1.23}$$

Here, $V_{II}(R)$ is the potential energy for the Ith electronic state, evaluated at the center of the Gaussian basis function.

In AIMS, the nuclear wavefunction is informed by electronic structure calculations *on-the-fly*. In order to determine the forces acting on the nuclei, gradients of the electronic potential energy surfaces are computed. Throughout the propagations, *non-adiabatic* coupling calculations are performed between the state that the trajectory propagates on and all other electronic states. The sampling of the initial position and momenta are taken from a ground state Wigner distribution where initially the set of sampled trajectories are all coupled via the coefficients multiplying them. An approximation can be made such that all parent basis functions are decoupled, the *so-called* initial first generation (IFG) approximation. This is possible because the initially sampled basis functions rapidly spread out from the initial region of sampling, thus de-coupling from each-other. The IFG thus restricts all spawned basis functions to be only coupled to parent basis functions, negating the need to propagate the entire basis in concert.

1.5 Simulation of Time-resolved Photoelectron Spectroscopy (TRPES)

The previous section demonstrated how the time-evolution of a wavepacket can be simulated, however, a time-evolving wavepacket is not an experimental observable. A wavepacket is a coherent superposition of states by which the molecular system can be represented and which is prepared by a coherent laser pulse. Experimentally, a femtosecond laser prepares a molecular wavepacket which can be interrogated and provide useful information about the molecule following photoexcitation. Here,

the focus will be on *time*-resolved experiments where the vibrational and electronic degrees of freedom of an evolving wavepacket are probed.

A typical time-resolved experiment employs a *pump-probe* scheme whereby an initial *pump* laser pulse prepares the excited state wavepacket and is followed by a time-delayed probe pulse which gives rise to the time-evolving signal. There exist many methods that employ a pump-probe scheme where the distinction can be made on the observable that is produced. In methods such as transient absorption spectroscopy (TAS)[18], the pump-probe observable is a photon that correlates to the measured absorption of light or transmittance by the sample as a function of time. The method that pertains to this body of work is time-resolved photoelectron spectroscopy (TRPES)[19] where the observable is an outgoing photoelectron produced by a probe laser pulse. Photoelectron spectroscopy is used as a probe for a few important reasons. There exist relaxed selection rules for photoionization and therefore ionization of a molecule is almost always an allowed process. The outgoing electron has an associated angular momentum and kinetic energy that can be detected, with the intensity of the observable corresponding to the overlap between the initial neutral and final cationic states. Additionally, the cationic states that are produced by the probe pulse have been well studied for a variety of molecules and molecular fragments[20].

1.5.1 Time-resolved photoelectron spectroscopy (TRPES)

A molecule in its ground electronic state (S_0) is excited to a manifold of electronic states (S_n, n=1,2...) via a pump laser pulse at an initial time (t_0). Following some time delay (Δt), the molecule undergoes vibrational motion and is interrogated by the probe pulse at time $t_0 + \Delta t$, ionizing the molecule and producing photoelectrons with a time-dependent kinetic energy spectrum, $\sigma(E,t)$.

To calculate a TRPES spectrum from AIMS data, ionization is considered from a manifold of N-electron states $\psi_I(\mathbf{r};\mathbf{R})$ to a set of (N-1)-electron states $\psi_\alpha(\mathbf{r};\mathbf{R})$. At a given time, the total photoelectron signal, $\sigma(E,t)$ is approximated by taking a sum of of the probabilities of ionization $W_{1\alpha}$ evaluated at the centers of each trajectory Gaussian basis function ($\bar{R}^I_{\rho_j}$):

$$\sigma(E,t) = \sum_{I=1}^{n_s^0} \sum_{\alpha=1}^{n_s^+} \sum_{j=1}^{N_I} |C_j^I(t)|^2 \times W_{1\alpha}(\bar{R}^I_{\rho_j}) \delta(E - (\omega - \Delta E_I^\alpha(\bar{R}^I_{\rho_j}(t)))) \tag{1.24}$$

The $C_j^I(t)$ terms are taken from the AIMS basis functions, where the AIMS densities $|C_j^I(t)|^2$ are used to construct the observable. The bounds on the first two summations dictate the number of neutral (n_s^0) and cationic (n_s^+) states respectively, while the final summation has bound over the total number of electronic states. Here ω denotes the energy of the laser pulse and ΔE_I^α is the energy difference between the neutral and cationic state. It has been demonstrated previously that the relative probability of ionization $W_{I\alpha}$ is proportional to the squares of the norms of the Dyson orbital $\phi_{I\alpha}^D$[21]:

$$\phi_{I\alpha}^D = \sqrt{N}\,\langle \psi_I(\mathbf{r};\mathbf{R})|\psi_\alpha(\mathbf{r};\mathbf{R})\rangle \tag{1.25}$$

The Dyson orbitals correspond to the projection of an N-electron wavefunction on to an (N-1)-electron wavefunction that produces a function consisting of one electron.

The individual calculated spectra are convoluted in the time-domain with a Gaussian function whose full width at half maximum (FWHM) corresponds to the experimental cross-correlation between the pump and probe laser pulses. To account for the resolution of the experimental spectra, the calculated spectrum is convoluted in the energy domain using a Gaussian function with a FWHM on the order of 0.05-0.15 eV.

Chapter 2

Cyclopropane

2.1 Preamble

The results of this study have been summarized in and adapted from the following paper Coates, M. R.; Larsen, M. A. B.; Forbes, R.; Neville, S. P.; Boguslavskiy, A. E.; Wilkinson, I.; Sølling, T. I.; Lausten, R.; Stolow, A.; Schuurman, M. S. "*Vacuum ultraviolet excited state dynamics of the smallest ring, cyclopropane. II. Time-resolved photoelectron spectroscopy and ab initio dynamics.*" J. Chem. Phys., **2018**, *149* (14), 144311. in conjunction with Part I: Neville, S. P.; Stolow, A.; Schuurman, M. S. "*Vacuum ultraviolet excited state dynamics of the smallest ring, cyclopropane. I. A reinterpretation of the electronic spectrum and the effect of intensity borrowing.*" J. Chem. Phys. **2018**, *149* (14), 144310.

The contributions that I made to the paper were the calculation and simulation of a theoretical results and the organization, writing and submission of the paper. In what follows, all experimental results were collected by M. A. B. Larsen and R. Forbes. The initial populations that guided the trajectories were taken from the work done by S. P. Neville in Part I of the study. The contributions to the development of the experimental setup were noted and given to A. E. Boguslavskiy, I. Wilkinson and R Lausten. The supervision of the experimental work was conducted by A. Stolow and T. I. Sølling, while the theoretical supervision was conducted by M. S. Schuurman.

2.2 Abstract

The vacuum-ultraviolet (VUV) photoinduced dynamics of cyclopropane (C_3H_6) were studied using time-resolved photoelectron spectroscopy (TRPES) in conjunction with *ab initio* quantum dynamics simulations. Following excitation at 160.8 nm, and subsequent probing via photoionization at 266.45 nm, the initially prepared wavepacket is found to exhibit a fast decay (<100 fs) that is attributed to the rapid dissociation of C_3H_6 to ethylene (C_2H_4) and methylene (CH_2). The photodissociation process proceeds via a concerted ring opening and C-C bond cleavage in the excited state. *Ab initio* multiple spawning (AIMS) simulations indicate that ring-opening occurs prior to dissociation. The dynamics simulations were subsequently employed to simulate a TRPES spectrum, which was found to be in excellent agreement with the experimental result. On the basis of this agreement, the (i) fitted time constants of 35 ± 20 and 57 ± 35 fs were assigned to prompt dissociation on the lowest-lying excited state, prepared directly by the pump pulse, and (ii) non-adiabatic relaxation from higher-lying excited states that lead to delayed dissociation, respectively.

2.3 Introduction

The photochemistry of cyclopropane and its substituted derivatives has been studied extensively for its use in synthetic organic chemistry[22–24]. This moiety is often bonded to larger chromophores in organic synthesis and facilitated isomerization and ring-expansion[22] upon irradiation with deep-ultraviolet radiation (up to 6.7 eV)[25–28]. As the smallest organic ring, the excited states of cyclopropane and the cyclopropane radical cation have been of interest for many years, with previous studies focusing on vibronic coupling in the lowest-energy excited states[29–31]. This is especially true of the cyclopropyl radical cation, which has been a subject of study for more than 45 years[32–35]. Despite the extensive literature describing the photochemistry of cyclopropane, to our knowledge there exist no time-resolved studies of the excited state dynamics of this molecule.

Previous gas phase studies have shown that photolysis of cyclopropane occurs in the VUV for excitation energies ranging from 7.6-10.0 eV[36–39]. These reports highlight that branching between numerous reaction pathways can result, including the dissociation of cyclopropane to yield ethylene and the methylene radical:

$$\text{c-}C_3H_6 \xrightarrow{h\nu} C_2H_4 + CH_2 \tag{2.1}$$

In one study, this pathway was found to account for 69% of the photoproducts following excitation at 163.4 nm[38]. The three remaining pathways observed are CH_3 + C_2H_3 (17%), H-loss (14%) and H_2 formation (1%). Here we consider excitation with 160.8 nm (7.71 eV) photons that populate a range of electronically excited states well above the C_2H_4+CH_2 dissociation threshold that is estimated to occur at 3.72 eV[39].

The ground state electronic configuration of cyclopropane is given by:

$$[\text{core}](2a_1')^2(2e')^4(1a_2'')^2(3a_1')^2(1e'')^4(3e')^4$$

where the highest occupied molecular orbital (HOMO), 3e′, is a C-C σ-bonding orbital, and the lowest energy virtual orbitals are of $3s(a_1')$, $3p_z(a_2'')$, and $3p_{x/y}(e')$ Rydberg character. For the sake of brevity, here and in the following, the label $3p_{x/y}$ is used as a shorthand for $3p_x/3p_y$. The identity of the $E'\sigma(3s)$ state as the lowest-lying state was confirmed by one- and two-photon absorption measurements[40]. While transition to the σ3s Rydberg state is dipole-allowed, the low oscillator strength of the transition has made experimental characterization of this state challenging. This transition has been observed in the 6.5-6.8 eV region both by direct absorption[40, 41] and by resonance enhanced multi-photon ionization[31, 40], but with low intensity.

The two lowest-lying dipole allowed absorption bands with significant oscillator strength have their onset at 7.1 eV and exhibit broad maxima centered at 7.9 and 8.6 eV[42, 43]. These two bands were attributed to the two Jahn-Teller (JT) split components of the $E'(\sigma 3p_{x/y})$ state. Previous assignments of the absorption spectrum have, however, neglected the effects of vibronic coupling. In a companion publication to this article[44], new calculations of the absorption spectrum, which explicitly include the effects of vibronic coupling between the excited states, are presented. There it is conclusively demonstrated that intensity borrowing from the optically bright $E'(\sigma 3p_{x/y}) \leftarrow S_0$ transition by the dipole-forbidden $A_1'(\sigma 3p_{x/y}) \leftarrow S_0$ and $A_2'(\sigma 3p_{x/y}) \leftarrow S_0$ transitions gives rise to the majority of the intensity in the first two bands of the absorption spectrum. As discussed below, this new assignment of the spectrum has important implications for the analysis of the electronic character of the wavepacket prepared following photoexcitation.

In the following, we present a joint experimental and theoretical study of the dynamics of cyclopropane following photoexcitation at 160.8 nm and using time-resolved photoelectron spectroscopy (TRPES)[19] to probe the evolution of the excited state wave packet. *Ab initio* multiple spawning (AIMS) computations are employed to both elucidate the underlying vibronic dynamics as well as simulate the TRPES spectrum.

2.4 Experimental and Theoretical Methods

2.4.1 Experimental

The femtosecond VUV pulse generation scheme employed in these experiments was described in detail previously[45]. In short, the laser system (Coherent Legend Elite Duo) employed throughout these experiments delivered 7.5 mJ pulses at 1 kHz, with a central frequency of 800 nm. A 3.25 mJ component of the total laser output was split to generate the pump and probe arms. The probe arm was frequency tripled by sum frequency mixing in two consecutive BBO crystals, allowing for energies of 1 μJ per pulse. The pump was generated by four-wave mixing in Ar gas[46]. Specifically, the pump arm is split into two paths; one part was frequency tripled to 266 nm by a pair of consecutive BBO crystals and the other part is left as the fundamental at 800 nm. The resulting beams were focused and overlapped in a non-collinear fashion in an Ar gas cell, held at 43 mBar, to generate the 160.8 nm pump pulse and yield an energy per pulse close to 0.5 μJ. A set of dichroic mirrors having high reflectivity at 160 nm and high transmission at 266.45 nm and 800 nm were used to separate the residual driving beams in the wave mixing process and for subsequent recombination of the pump and probe laser pulses.

The pump and probe beams were mildly focused and collinearly combined along the optical axis of a velocity map imaging (VMI)[47]. Along this axis, the beams passed through a set of input baffles, the sample molecular beam, and a set of exit baffles. The baffles were incorporated in the spectrometer to help minimize the electron signals associated with scattered UV/VUV light. The pump-probe delay at the sample was controlled by a motorized delay stage (Newport XML210). The temporal overlap of the pump and probe pulses was found via non-resonant $1+1'$ ionization of Xe. The time resolution was determined by fitting a Gaussian function to the temporal dependence of the the non-resonant electron yield which resulted

in a cross-correlation duration of 105 fs full-width at half-maximum (FWHM). The splitting of the $^2P_{3/2}$ and $^2P_{1/2}$ lines in the ionic ground state in Xe also served as a spectrometer energy calibration. The molecular beam was generated in a source chamber by expansion of a 5 % mix of cyclopropane in He through an Even-Lavie valve at a stagnation pressure of 2 Bar. The supersonic molecular beam was skimmed before entering the light-molecular beam interaction chamber and a stack of open aperture electrostatic lens plates. The molecular beam was injected along the axis of photoelectron projection, perpendicular to the pump and probe laser beam propagation. The accelerated photoelectrons were detected by a Microchannel Plate (MCP)-Phosphor detector with the images recorded using a Charge-Coupled Device (CCD) camera. The recorded images were processed by a matrix inversion method [48] to obtain the inverse Abel transform. However, ionization of residual gas in the interaction chamber produced a non-negligible background signal which was corrected for by dynamically recording the background signal between gas pulses. This was done at each pump-probe delay for each scan in order to account for any time-dependent background signals. 30 identical scans of the pump-probe delay were averaged to produce the presented spectra.

2.4.2 *Ab initio* multiple spawning calculations

In AIMS method[15–17], the wavefunction *ansatz* is given by

$$|\Psi(\boldsymbol{R},\boldsymbol{r},t)\rangle = \sum_{I=1}^{n_s} |\psi_I(\boldsymbol{r},\boldsymbol{R})\rangle\, |\chi_I(\boldsymbol{R},t)\rangle\,. \tag{2.2}$$

Here, $\boldsymbol{r}$ and $\boldsymbol{R}$ denote the electronic and nuclear coordinates, respectively. The $|\psi_I(\boldsymbol{r},\boldsymbol{R})\rangle$ denote the adiabatic electronic states, and $|\chi_I(\boldsymbol{R},t)\rangle$ is the nuclear wavefunction for the Ith electronic state. The nuclear wavefunctions are in turn expanded in terms of frozen Gaussian basis functions $\left|g_j^I\right\rangle$:

$$|\chi_I(\boldsymbol{R},t)\rangle = \sum_{j=1}^{N_I(t)} C_j^I(t) \left|g_j^I(\boldsymbol{R};\bar{\boldsymbol{R}}_j^I(t),\bar{\boldsymbol{P}}_j^I(t),\gamma_j^I(t),\alpha_j^I)\right\rangle. \tag{2.3}$$

Each Gaussian basis function depends parametrically on a time-dependent centroid position, $\bar{\boldsymbol{R}}_j^I$, momentum, $\bar{\boldsymbol{P}}_j^I$, and phase, γ_j^I, as well as a time-independent width, α_j^I. The positions and momenta are taken to evolve classically while the phases are propagated according to semi-classical equations of motion (EOMs)[49]. The EOMs for the expansion coefficients C_j^I are determined variationally via the solution of

the time-dependent Schrödinger equation. The number of Gaussian basis functions, $N_I(t)$, is time-dependent, with new basis functions created, or spawned, in regions of large derivative coupling in order to describe non-adiabatic transitions between adiabatic electronic states[49].

2.4.3 Time-Resolved Photoelectron Spectroscopy Simulations

We consider ionization from a set $\{|\psi_I\rangle : I = 1, \ldots, n_s^0\}$ of N-electron states to a set $\{|\psi_\alpha\rangle : \alpha = 1, \ldots, n_s^+\}$ of $(N-1)$-electron states. We model the TRPES data as an incoherent sum of contributions from the relative probabilities of ionization, $W_{I\alpha}$, evaluated at the centres $\bar{\boldsymbol{R}}_j^I$ of the Gaussian basis functions in the AIMS dynamics calculations:

$$\sigma(E,t) = \sum_{I=1}^{n_s^0} \sum_{\alpha=1}^{n_s^+} \sum_{j=1}^{N_{I(t)}} \left|C_j^I(t)\right|^2 W_{I\alpha} \delta\left(E - \left(\omega - \Delta E_{I\alpha}(\bar{\boldsymbol{R}}_j^I(t))\right)\right). \tag{2.4}$$

Here, ω denotes the probe photon energy, and $\Delta E_{I\alpha}$ is the vertical energy difference between the states $|\psi_I\rangle$ and $|\psi_\alpha\rangle$. The δ-function arises because we assume vertical ionization to occur. To proceed, we take the relative probabilities of ionization, $W_{I\alpha}$, to be proportional to the squares of the corresponding Dyson orbital norms, $\phi_{I\alpha}^D$:

$$W_{I\alpha} \propto ||\phi_{I\alpha}^D||^2, \tag{2.5}$$

$$\phi_{I\alpha}^D = \sqrt{N}\,\langle\psi_I|\psi_\alpha\rangle\,. \tag{2.6}$$

The approximation in Eq. 2.5 is known to hold well in the case of weak field ionization[50], which is the situation considered in the present study.

The calculated TRPES data is convoluted with a Gaussian using a FWHM of 105 fs in the time domain and 0.23 eV in the energy domain. The time and energy convolutions correspond to the respective duration and energy spreads of the experimental pump and probe laser pulses, as determined in the cross-correlation measurements.

2.4.4 Computational details

In the AIMS calculations, the adiabatic energies, energy gradients and non-adiabatic couplings required to evaluate the EOMs were calculated at the multi-reference first-order configuration interaction (MR-FOCI) level of theory. The reference configurations and orbitals were taken from a complete active space self-consistent-field (CASSCF) calculation employing an active space including the orbitals $3e'(\sigma)$, $4a_1'(3s)$, $2a_2''(3p_z)$, and $4e'(3p_x, 3p_y)$. We denote this level of theory by CAS(4,6). In the CAS(4,6) calculations, state averaging was performed over the nine lowest singlet states, corresponding to $A_1'(\sigma^2)$, $E'(\sigma 3s)$, $E''(\sigma 3p_z)$, $A_2'(\sigma 3p_{x/y})$, $A_1'(\sigma 3p_{x/y})$, and $E'(\sigma 3p_{x/y})$ at the Franck-Condon (FC) point. The level of theory is denoted by MR-FOCI(4,6). The aug-cc-pVDZ basis was used in all calculations. All electronic structure calculations were performed using the COLUMBUS set of programs[51].

Initial positions and momenta were sampled from the harmonic ground vibrational state Wigner distribution, with the required normal modes and frequencies being calculated at the CCSD(T)/cc-pVTZ level of theory using the CFOUR set of programs[52]. A total of 25 initial basis functions were used with each propagated independently under the so-called independent first generation approximation[49]. A propagation time of 400 fs was used. At the end of the AIMS simulations, a total of 1260 basis functions had been spawned.

As a result of the limited accuracy of the computationally tractable MR-FOCI(4,6) calculations used in the AIMS calculations, the vertical ionization energies $\Delta E_{I\alpha}$ used in the simulation of the TRPES data are not sufficiently accurate to be used on their own. To correct for this, a constant shift of these terms was applied such that the calculated FC point S_1-to-D_0 ionization energy was brought into agreement with the value calculated at a higher level of theory. Specifically, this shift was calculated using energies calculated at the equation-of-motion coupled-cluster with single and double excitations (EOM-CCSD) level using the aug-cc-pVTZ basis. All EOM-CCSD calculations were performed using the CFOUR program[52].

2.5 Experimental Results

We present our experimental TRPES results, which are then compared to the AIMS simulations in a following section. The pump (7.71 eV) and probe (4.65 eV) pulses combine to give a total photon energy of 12.36 eV, yielding the D_0 and D_1 cation

states as open channels[53]. The adiabatic ionization energy of cyclopropane is 9.86 eV [54–56] and therefore a maximum photoelectron kinetic energy of 2.5 eV is expected. Fig. 2.1(a) shows the TRPES spectrum measured following excitation at 7.71 eV. The spectrum exhibits two broad maxima, centered at 1.3 eV and 1.9 eV, which exhibit different temporal dynamics as a function of pump-probe delay. The integrated photoelectron signals and the timescales associated with the two bands are qualitatively very clear from the transients shown in Fig. 2.1(b). A time delay between the appearance of the two peaks in the TRPES data can clearly be seen. This could be interpreted as the initially excited state undergoing fast internal conversion (IC) to a lower excited state[57] and/or energy-lowering structural dynamics occurring within the initially excited state.

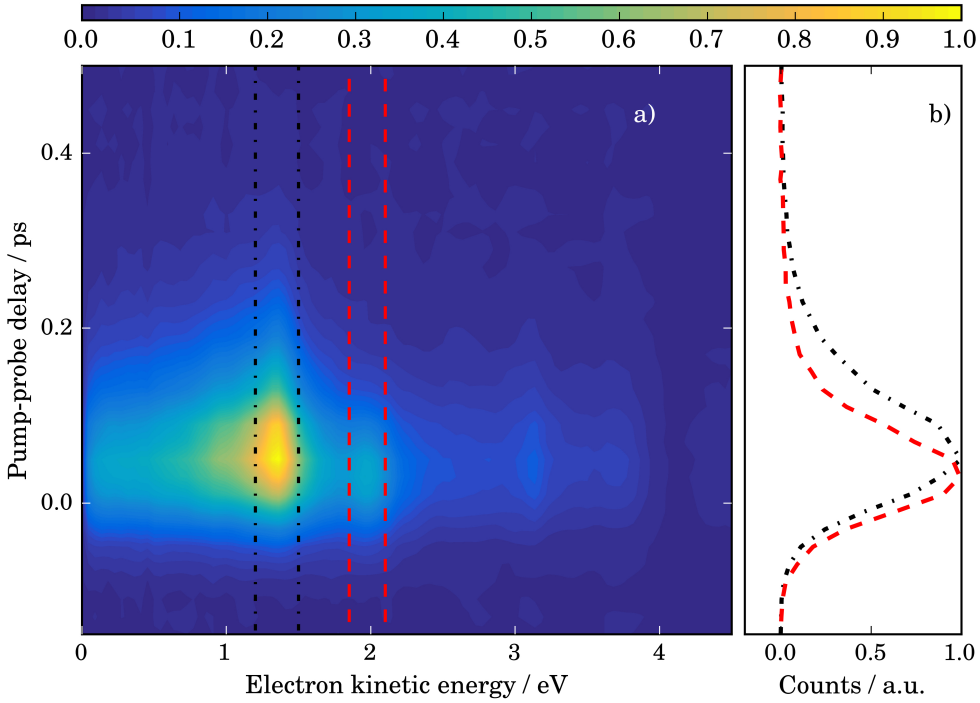

Figure 2.1: (a) Time-resolved photoelectron spectroscopy (TRPES) spectrum of cyclopropane recorded using pump and probe wavelengths of 160.8 nm and 267 nm, respectively. (b) integrated energy regions (black and red vertical lines) showing the pump-probe delay dependent yields.

A 2D global fitting procedure was employed to investigate the detailed time-dependence of the photoelectron signal. We used the Levenberg-Marquardt fitting routine, with the experimental data ($S(E, \Delta t)$) described[58] by the following expression:

$$S(E, \Delta t) = \sum_{i=1}^{n} A_i(E) \cdot P_i(\Delta t) \otimes g(\Delta t), \tag{2.7}$$

where E is the kinetic energy of the photoelectron, Δt is the pump-probe time-delay, $g(\Delta t)$ is the experimental Gaussian instrument response or cross-correlation function (105 fs FWHM) and $A_i(E)$ is the amplitude profile of the decay-associated photoelectron spectrum (DAS) of the ith decay channel with time-dependence $P_i(\Delta t) = \exp(-\Delta t/\tau_i)$. The global fit yielded two time-constants (i.e. $n = 2$) displayed in Table 2.1; τ_1=35±20 fs for the decay of the high kinetic energy peak and τ_2=57±35 fs for the decay of the low kinetic energy peak. The DAS are shown in Fig. 2.2. The negative amplitude in the DAS associated with the 35 fs time constant has negative values around 1.3 eV, whilst the DAS for the 57 fs time constant has positive values in this region. This is a clear indication of a sequential process in which the initial wavepacket decays on a timescale of τ_1=35 fs to a lower-energy state and/or nuclear coordinate distribution that in turn has a lifetime of τ_2=57 fs.

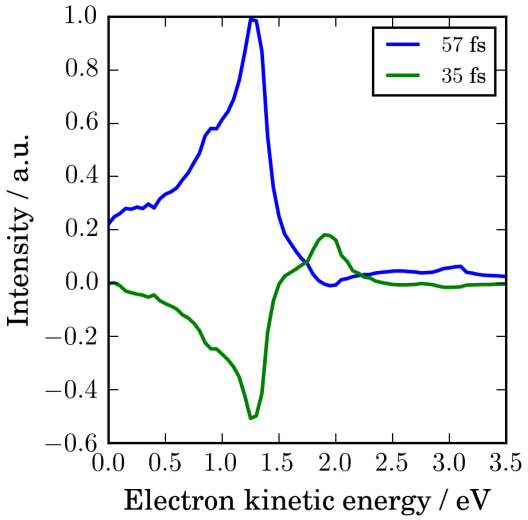

Figure 2.2: Decay associated spectra from the 2D global fit to the experimental TRPES data. The negative amplitude associated with the 35 fs time constant is a clear indication of a sequential process.

	Experimental	Theoretical
τ_1 (fs)	35 ±20	43 ±20
τ_2 (fs)	57 ±35	65 ±30

Table 2.1: Decay constants τ_1 and τ_2 from the 2D global fits to the experimental and simulated TRPES data. The error bars correspond to a 95% confidence interval from the 2D global fitting procedure.

State	Symmetry	Character	ΔE (eV)
S_1	$^1E'$	$\sigma 3s$	6.73
S_2	$^1E''$	$\sigma 3p_z$	7.19
S_3	$^1A'_2$	$\sigma 3p_{x/y}$	7.30
S_4	$^1A'_1$	$\sigma 3p_{x/y}$	7.33
S_5	$^1E'$	$\sigma 3p_{x/y}$	7.35

Table 2.2: Vertical excitation energies at the Franck-Condon point calculated at the MR-FOCI(4,6)/aug-cc-pVDZ level of theory.

2.6 Theoretical Results

2.6.1 Potential energy surfaces

Table 2.2 lists the vertical excitation energies of the first 5 singlet excited states calculated at the MR-FOCI/aug-cc-pVDZ level of theory. To assess the accuracy of the electronic structure method employed in the dynamics simulation, particularly the impact of employing a large (nine-) state average in the MCSCF computation, we will compare vertical excitation energies to the high-level aug-cc-pVTZ / CC3 and aug-cc-pVTZ / EOM-CCSD computations in Ref. [44]. This comparison shows that the present vertical excitation energies differ from the benchmark level computations by ≈ 0.9 eV. This difference arises from the difficulty of the MR-FOCI wavefunction to describe the differential correlation effects between the valence ground state and Rydberg excited state manifold. However, the dynamics of interest will be more sensitive to relative errors in energy *between* the excited states. On this metric we see that the energies between the two methods are in quantitative agreement, with the MR-FOCI and CC3 and EOM-CCSD results displaying differences of ≈0.01 eV between the relative energies of the relevant excited states.

The first excited state is the $E'(\sigma 3s)$ state. At ≈ 0.45 eV above this energy

lies a manifold of 4 electronic states that span only 0.66 eV. In order of increasing energy, these are the $^1E''(\sigma 3p_z)$, $^1A_2'(\sigma 3p_{x/y})$, $^1A_1'(\sigma 3p_{x/y})$ and $^1E'(\sigma 3p_{x/y})$ states. Upon JT distortion, the doubly-degenerate states split, yielding a total of 8 non-degenerate excited adiabatic states. In the context of the excited state dynamics, the most important JT active modes correspond to asymmetric ring stretching and ring bending motions. Here, we will focus primarily on two nuclear degrees of freedom which serve to represent the dynamics involved: the angle bending coordinate, q_θ, and the CH_2 dissociation coordinate, q_{dissoc}. The definitions of these coordinates are given in Fig. 2.3.

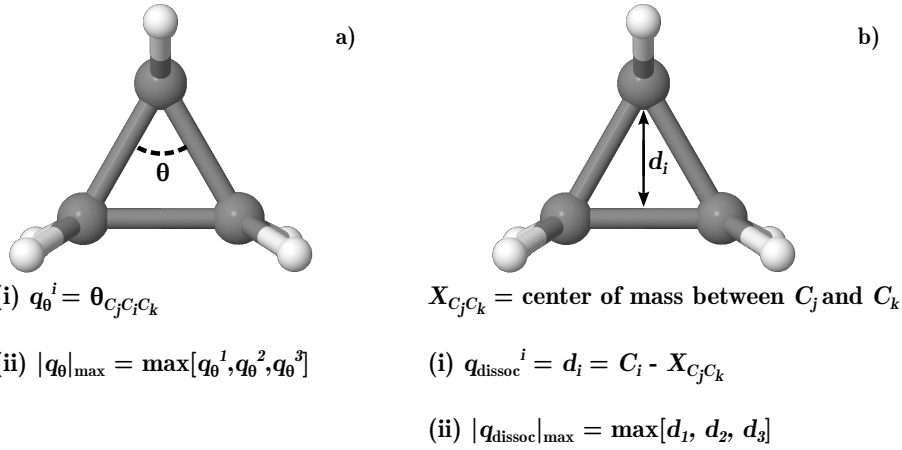

Figure 2.3: The angle bending and dissociation coordinate definitions (a)(i) and (b)(i) respectively, were used to construct the potential energy surface cuts in Fig. 2.4. The maximum of the angle bending and dissociation coordinates as defined in (a)(ii) and (b)(ii) respectively, were used for all nuclear wavepacket dynamics analyses in Fig. 2.5 and Fig. 2.8.

Fig. 2.4 shows the adiabatic potential energy surfaces (PESs) as a function of $\mathbf{q}_\theta$ and $\mathbf{q}_{\text{dissoc}}$, calculated at the MR-FOCI(4,6)/aug-cc-pVDZ level of theory. The lower adiabatic surfaces display barrierless large amplitude motion along these JT-active coordinates. For example, from Fig. 2.4(a), highlights a flat potential energy profile with increasing $\mathbf{q}_\theta$ for the S_1-S_4 adiabatic states, suggesting energetically barrierless ring-opening may occur. Perhaps most importantly with regards to the excited state dynamics, as is shown in Fig. 2.4(b), the vertical excitation energies of all excited states lie above the barrier to the formation ethylene (C_2H_4) and methylene (CH_2) in the S_1 state. Accordingly, dissociation would proceed promptly following population transfer to the S_1 state.

As evinced by Fig. 2.4(b), the potential energy surfaces employed in the dynamics simulations have minor discontinuities along the dissociation coordinate. These

arise due to the σ^* orbital rotating into the large active space. While the classical energy of the trajectories in the simulation were conserved to 10^{-5} a.u., this discontinuity manifested as a small energy jump in the dissociation exit channel. Those trajectories undergoing this energy jump (exclusively on the adiabatic S_1 excited state) universally corresponded to dissociated products and were thus subsequently terminated.

2.6.2 Photo-excitation: initial state populations

Cyclopropane possesses a high density of low-lying vibronically coupled electronic states. In such a case, the initial state(s) prepared by a given pump pulse cannot be reliably estimated via an analysis of electronic transition dipoles and vertical excitation energies alone. The reason for this is that intensity borrowing effects may be operative, potentially leading to the population of optically dark electronic states. Indeed, our recent calculations, as discussed in the companion article[44], show that most of the intensity in the first two bands of cyclopropane's electronic absorption spectrum arise due to intensity borrowing from the optically bright $^1\mathrm{E}'(\sigma 3\mathrm{p}_{\mathrm{x/y}})$ state by the lower-lying optically dark states. Therefore, vibronic coupling effects must be included when estimating the initial state populations prepared by the experimental pump pulse. To do so, a model linear vibronic coupling Hamiltonian[59–61] was constructed which includes all first-order vibronic coupling terms between the first nine electronic states of cyclopropane. Initial state populations were then calculated by using the model Hamiltonian for a wavepacket propagation calculation in which an initial ground state wavefunction was coupled to the excited state manifold via a laser pulse. By using a laser pulse parameterized to match the experimental pump pulse, the electronic state populations at the end of the wavepacket propagation can be taken as estimates of the initial state populations prepared by the pump pulse. The wavepacket propagation calculations were performed using the multiconfigurational time-dependent hartree (MCTDH) method[62] using a nine-state, nine-mode model. The details of these calculations and the model Hamiltonian are given in the supplementary information of Ref. [44].

Using this approach, we found that only the S_1, S_2, S_3, and S_4 states are appreciably populated following excitation at 160.8 nm. This result is in direct contradiction with an analysis relying solely on transition dipole moments and vertical excitation energies, which would predict that the $^1\mathrm{E}'(\sigma 3\mathrm{p}_{\mathrm{x/y}})$ is the initially prepared excited

state. We do, however, have confidence in our results as the model Hamiltonian used is found to reproduce the experimental absorption spectrum to a high degree of accuracy[44]. Accordingly, in the following we only consider excitation to these four states. The calculated relative populations of these states generated by the pump pulse are 0.33, 0.12, 0.30, and 0.25, respectively.

2.6.3 Wave packet dynamics simulation

Guided by the initial state populations calculated from the MCTDH calculations, AIMS simulations were performed with initial states corresponding to each of the S_1, S_2, S_3, and S_4 states.

Each wavepacket propagation was performed independently, and the results incoherently averaged using weights corresponding to the calculated initial state populations to give the final results. We first consider the one-dimensional reduced nuclear densities calculated from the AIMS simulations. These were calculated using the Monte-Carlo procedure detailed in Ref. [63]. In Fig. 2.5(a), we show the calculated reduced densities for the angle bending coordinate as a function of time. It is predicted that ring opening occurs rapidly following photoexcitation, with direct ring opening first occurring within 50 fs. The remaining part of the wavepacket undergoes a single revival back to the FC region after 80 fs, but then subsequently delocalizes over a wide range of angles greater than 100 deg.

Fig. 2.5(b) shows the calculated reduced densities for the CH_2 dissociation coordinate. Similar to the ring bending coordinate, a bifurcation of the wavepacket is found to occur, with one component undergoing rapid dissociation in under 50 fs, and a second component undergoing a classical-like revival back towards the FC region before becoming delocalized along the dissociation coordinate. The horizontal dashed line in Fig. 2.5(b) marks the value of the dissociation coordinate beyond which the asymptotic region (dissociation limit) of the potential lies. Here, dissociation is defined as the distance between the centres of mass of the C_2H_4 and CH_2 fragments being greater than $|\mathbf{q}_{\text{dissoc}}|_{\max} = 2.1$ Å. The picture which emerges is one in which CH_2 rapidly departs from a C_2H_4 co-fragment during a concerted ring-opening and bond stretching process.

Shown in Fig. 2.6(a) are the adiabatic state populations calculated from the AIMS simulations. The wave packet spans multiple electronic states, primarily $S_1 - S_4$. However, the population on S_3 and S_4 decays almost immediately to S_2 and

subsequently S_1. The latter displays a sudden increase in population around 25 fs corresponding to ring opened cyclopropane being transferred to S_1. Population on the ground adiabatic state begins to grow starting around 25 fs and continues to do so until the end of the simulation. Interestingly, there is a revival in S_2 population beginning around 50 fs which corresponds to a revival of the wavepacket to the FC region, which is characterized by smaller bond angles and bond lengths as shown in Fig. 2.5 around 80 fs.

Fig. 2.6(b) shows the calculated time-dependent probability of dissociation to form C_2H_4 and CH_2. It is predicted that cyclopropane begins to dissociate within 20 fs, and that dissociation is virtually complete by 250 fs. Finally, we note that the AIMS simulations predict that dissociation predominantly occurs on S_1, with population transfer to S_0 and S_2 largely occuring after the moleuclar system is already in the dissociation exit channel.

2.6.4 TRPES Simulation

The TRPES data calculated from the AIMS simulations is shown in Fig. 2.7(a). The calculated spectrum contains two peaks centered at 1.3 and 1.9 eV, in excellent agreement with the experimental TRPES data. A fit to the computed spectrum was performed using the same 2D global fitting algorithm employed in the analysis of the experimental spectrum (see Sec. III). The fit residuals of both the experimental and calculated TRPES data are included in the supplementary information. The time constants derived from the fits to both the experimental and calculated TRPES data are given in Table I. The agreement between the time constants derived from the calculated and experimental TRPES spectra is quantitative, and gives us confidence in the accuracy of the underlying AIMS dynamics simulations.

To shed light on the dynamical processes underlying the two time constants, we consider the contributions to the calculated TRPES data from: (i) the geometries at the centres of the Gaussian basis functions that contribute to each of the two bands, and (ii) the contribution of each electronic state to the TRPES data. In the following, we label the region around the band centered at 1.9 eV as region I and the region around the band at 1.3 eV as region II.

In Fig.2.7(b) to (e), we show the contributions to the calculated TRPES spectrum from each of the excited states S_1, S_2, S_3 and S_4. As the figure shows, the higher energy peak in region I is due almost exclusively to ionization of S_3 and S_4, whereas

the lower energy peak in region II contains contributions from all four adiabatic electronic states.

The two bands may be further characterized by analyzing the geometries $\bar{\boldsymbol{R}}_j^I$ at the centres of the Gaussian basis functions which give rise to the different regions in the calculated TRPES data. Specifically, for each Gaussian basis function contributing to the signal in each of region I and II, we determine the value of the internal coordinates $\mathbf{q}_\theta$, and $\mathbf{q}_{\text{dissoc}}$ at the centre of the basis function and histogram these values to determine the nuclear character of the wave packet giving rise to each each region. The results of this computation are shown in Fig. 2.8. It can clearly be seen that region I is characterized mainly by geometries in the vicinity of the FC region ($\mathbf{q}_\theta$ = 60 deg and $\mathbf{q}_{\text{dissoc}}$ = 1.4 Å). Conversely, we find that region II in the TRPES spectrum arises predominantly due to the components of the wavepacket corresponding to structures significantly displaced from the FC region. This is highlighted in Fig. 2.8 by a shift of the distribution to larger values of both internal coordinates.

2.7 Discussion

The AIMS simulations predict that the dynamics immediately following photoexcitation at 160.8 nm involve nuclear motion in each of the excited states, including barrierless ring-opening and large-amplitude C-C stretching vibrations. These structural deformations occur on all the prepared excited states ($S_1 - S_4$) and are accompanied by rapid non-adiabatic transitions to the lowest-lying adiabatic electronic states (S_1, S_2) from the higher-lying states (S_3, S_4). The population in the lower-lying states subsequently undergoes barrierless dissociation to produce C_2H_4 + CH_2. The ground electronic state population which begins to accumulate after about ∼30 fs is found to arise solely due to electronic relaxation in the dissociation exit channel, as described by Fig.2.6(b).

Significantly, each of these processes are encoded in the experimental TRPES data, and comparison with AIMS simulations allows the nature of the excited state dynamics to be extracted from these results. Based on the analysis of the simulated TRPES in terms of the underlying trajectory simulations in Section 2.6.4, the interpretation of the experimental TRPES that emerges is thus: the band in region I corresponds to ionization of the components of initially excited wave packet in states S_3 and S_4. Region II at short times corresponds exclusively to ionization from

S_1 and S_2 but this component of the wave packet rapidly dissociates. As the wave packet evolves, the population in the S_3 and S_4 states undergoes large amplitude structural relaxation, which increases the ionization potential (yielding lower kinetic energy electrons), and results in an increased signal in region II. This interpretation is confirmed by Fig. 2.8 which shows the lower energy band arising from more highly JT distorted geometries involving large amplitude motion corresponding to ring-opening and C-C bond elongation.

The timescale for dissociation (<100 fs) is captured by the time constant fits to both the experimental and simulated data. As the molecule undergoes barrierless dissociation to C_2H_4 + CH_2, the instantaneous vertical ionization potential increases until single-photon ionization is no longer possible with a 4.65 eV probe photon and the photoionization cross-section becomes correspondingly small. To be clear, the predicted photo-products from the proposed dynamical pathway cannot be ionized via one-photon ionization using the present pump-probe scheme, and are thus not readily observable in this experiment. However, the quantitative agreement between the experimentally determined time constants and the corresponding parameters extracted from spectrum generated from high level *ab initio* dynamics engender confidence in the present assignment. The main products observed in previous studies of the gas-phase photolysis, C_2H_4 + CH_2, have ionization energies of 10.40 eV[64] and 10.51 eV[65], respectively and would thus require ionization with 3 probe photons from their ground state. For the low probe laser intensities used in the current experiments, such channels were not observed.

The detailed results of our study are in general agreement with previous experimental studies which determined the photodissociation branching ratios following excitation at 163.4 nm[38]. In that report, the authors found that dissociation to C_2H_4 + CH_2 formed the dominant dissociation channel, accounting for 69% of the product yield. Three other channels observed involved the formation of CH_3+C_2H_3 (17% product yield), as well as H-loss (14%), and H_2 formation (1%). The investigators questioned whether the breaking of the C-C bonds to form the major dissociation products occurred simultaneously, or was preceded by ring-opening. Our results confirm that it is the latter: the excited molecule first undergoes large amplitude motion, which includes ring-opening, before ultimately dissociating.

We note that the simulations reported here have found C_2H_4 + CH_2 to be the *only* product channel accessed via photoexcitation. The present study was focused in the ultrafast excited state dynamics and did not as opposed to ground state

dynamics following the photodissociation process. The formation of C_2H_4 + CH_2 and other species via statistical dissociation from the hot ground state was not considered here.

2.8 Conclusion

The current study finds that the photoinitiated dynamics of cyclopropane, following excitation near the maximum of the lowest lying absorption band at 160.8 nm, are characterized by rapid ring opening and dissociation to ethylene and methylene. While both these motions are initiated immediately upon excitation, the shorter timescale for ring-opening ensures that this process precedes dissociation. On the basis of quantitatively accurate simulations of the absorption spectrum, we can definitively state that the wave packet prepared by the pump process is of mixed electronic character and arises due to the strong vibronic coupling between the optically bright $^1E'$ and the lower-lying Rydberg states. That component of the wave packet which is prepared directly on the lowest lying 3s (S_1) state dissociates promptly, whereas those components of higher excited electronic character first undergo nonradiative decay to the lower adiabatic states before dissociating. Interestingly, both the structural and electronic relaxation dynamics gives rise to distinct spectral features in the TRPES data, the assignment of which is enabled by high level *ab initio* simulations of the excited state dynamics and TRPES spectrum. Those components of the wave packet that correspond to higher-lying excited states at short times, prepared directly by the photoabsorption process, give rise to the photoelectron band at 1.9 eV, while a time delayed band around 1.3 eV arises following large amplitude nuclear displacements and non-radiative decay. The simulated spectrum shows that this lower-energy band also overlaps with the ionization signal from the initially prepared S_1 and S_2 states. The ethylene and methylene photoproducts are formed on the electronically excited S_1 state but, as previous studies have shown, any excited state C_2H_4 product will rapidly undergo internal conversion to the ground electronic state. The degree of agreement between the simulated and experimentally determined TRPES spectra is impressive, and has allowed for the unusually fine-grained assignment of all the main features of the time-resolved spectrum.

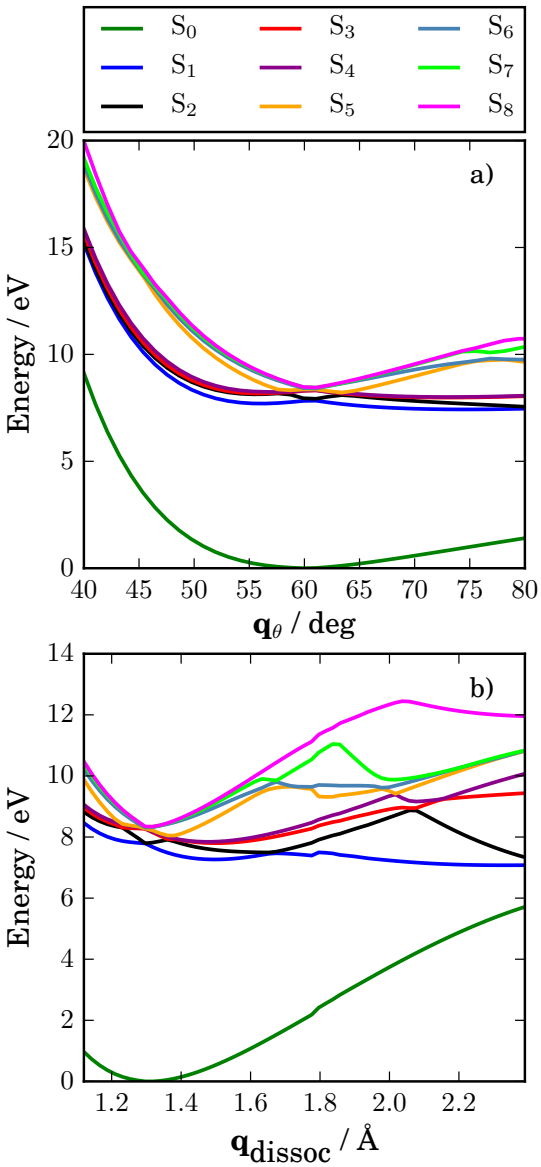

Figure 2.4: Potential energy surface cuts along internal coordinates (see text for definitions) relevant for the femtosecond timescale dynamics. Both coordinates lift the degeneracy and give rise to an energy-lowering displacement from the D_{3h} ground state minimum geometry. In particular, panel (b) shows that the energy of the FC point on the excited state surface lies above the C_2H_4 + CH_2 dissociation asymptote

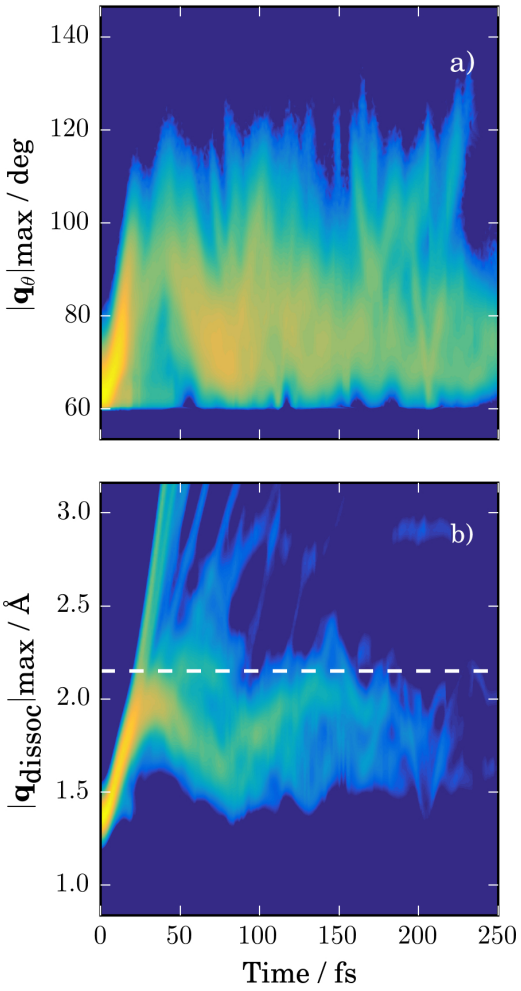

Figure 2.5: One dimensional reduced nuclear densities calculated from the AIMS simulations. (a) the angle bending coordinate. (b) The dissociation coordinate.

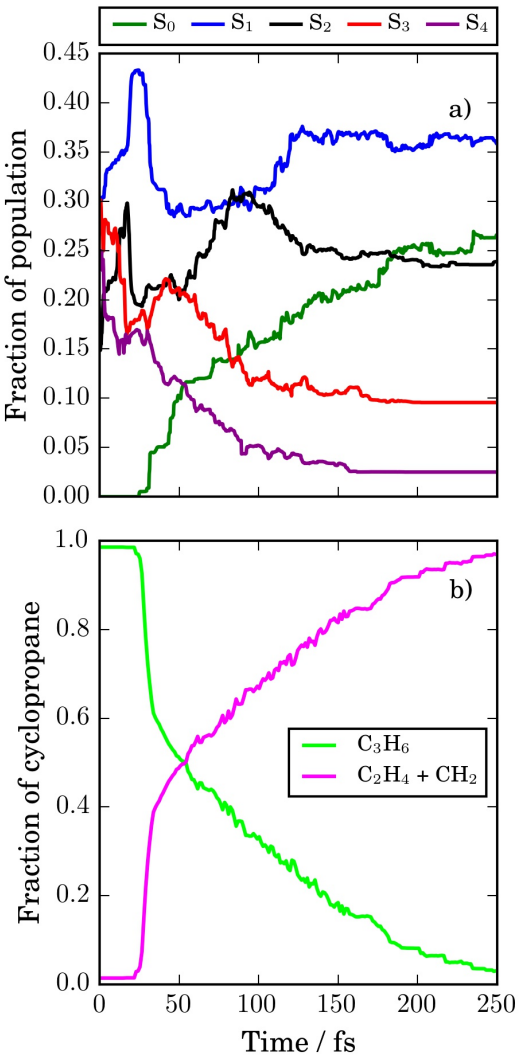

Figure 2.6: Panel (a) shows the time evolution of the adiabatic state populations as obtained from the AIMS simulation. Panel (b) illustrates the fraction of the wave packet characterized by molecular C_3H_6 vs. dissociated C_2H_4 and CH_2 as a function of time.

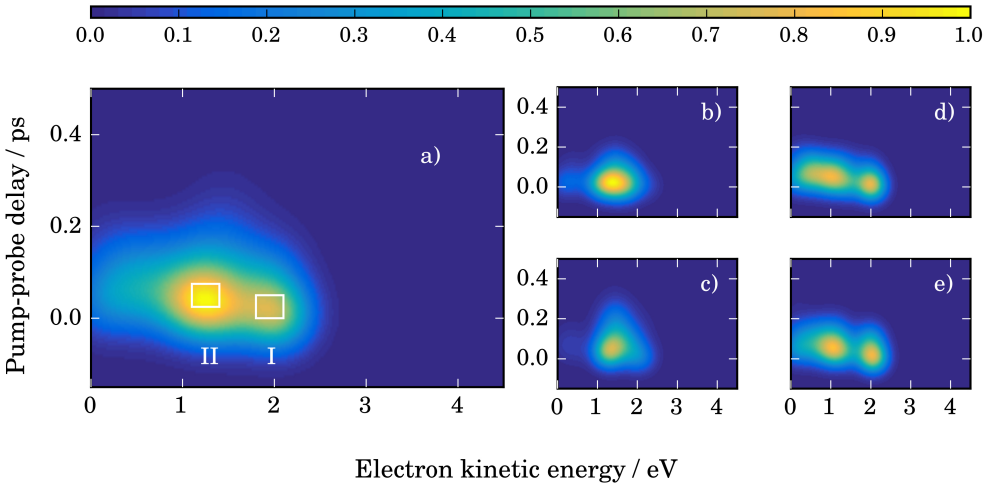

Figure 2.7: (a) TRPES data calculated from the results of the AIMS simulations. Shown alongside are the contributions to the total spectrum from each electronic state: (b) S_1, (c) S_2, (d) S_3, and (e) S_4. All spectra are displayed with the same colourmap.

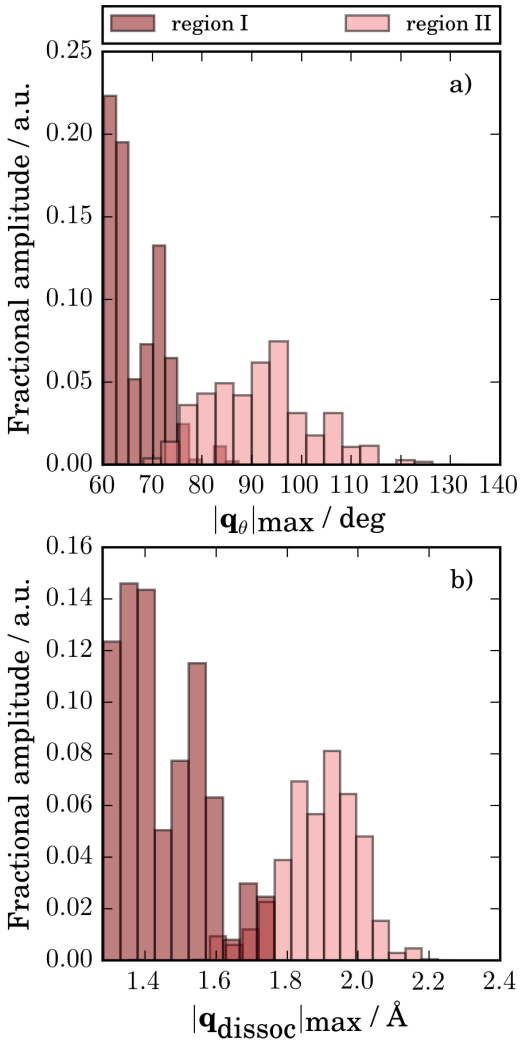

Figure 2.8: Geometrical distribution along coordinates associated with photoelectron energy regions I and II in the TRPES data. For details, see the text.

Chapter 3

Nitromethane

3.1 Preamble

All of the calculations and simulations in the work that follows was conducted by myself, with guidance from S. P. Neville and M. S. Schuurman. The results of this study will be summarized in a paper that will be submitted hereafter.

3.2 Abstract

The vacuum-ultraviolet (VUV) photoinduced dynamics of nitromethane (CH_3NO_2) have been studied by RASSCF electronic structure calculations and *ab initio* simulations. The requisite electronic structure calibrations permit the simulation of the dynamics following photoexcitation to the absorption maximum at 6.25 eV. The *ab initio* multiple spawning simulations indicate that major reaction pathway is the cleavage of the C-N bond: $CH_3NO_2 \xrightarrow{h\nu} CH_3 + NO_2$ on the S_1 and S_0 states. The results suggest that one minor pathway is likely to exist on the excited state corresponding to the oxygen loss, $CH_3NO_2 \xrightarrow{h\nu} CH_3NO + O$. The nitro-nitrite isomerization, $CH_3NO_2 \xrightarrow{h\nu} CH_3ONO$ pathway, is not observed on the excited state. The initially prepared wavepacket is shown to decay sequentially with S_2 population increasing within 10 fs and S_1 and S_0 population accumulating within 40 and 60 fs, respectively.

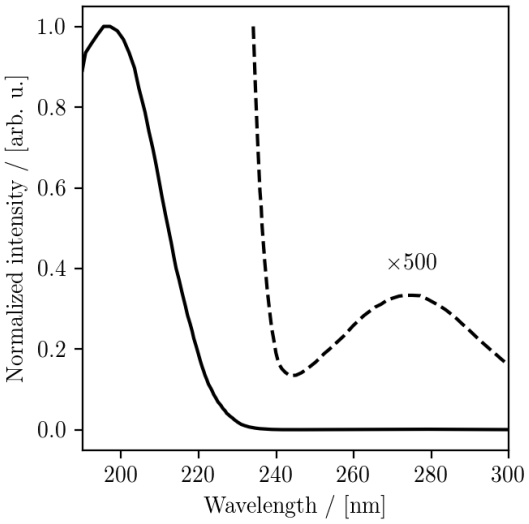

Figure 3.1: The UV absorption spectrum of nitromethane, adapted from Ref. [69]. The bold line indicates the strong $\pi \rightarrow \pi^*$ band centered at 198 nm. The dashed lines indicate the weak n $\rightarrow \pi^*$ transition, showing $\times 500$ the original intensity.

3.3 Introduction

The photochemistry of nitromethane has been studied extensively as a prototypical nitro substituted hydrocarbon. Previous studies that have attempted to elucidate the possible photodissociation pathways upon irradiation with vacuum-ultraviolet radiation at 198 nm. The ultraviolet absorption spectrum of nitromethane contains two bands, shown in Fig. 3.1, the dominant $\pi \rightarrow \pi^*$ at 198 nm and the weak $n \rightarrow \pi^*$ transition at 275 nm[66]. The $\pi \rightarrow \pi^*$ transition is localized on the NO_2 moiety[67], while the $n \rightarrow \pi^*$ transition occurs from a non-bonding electron on the oxygen atom[68].

To date, experimental studies have shown that the major reaction pathway is involves the cleavage of the C-N bond that is independent of excitation wavelength:

$$CH_3NO_2 \xrightarrow{h\nu} CH_3 + NO_2 \tag{3.1}$$

There is considerable debate over the existence and ratio of a number of minor pathways in the photodissociation of nitromethane. Most recently, a femtosecond pump-probe photolysis and time-of-flight mass spectrometry (TOFMS) study[70] has assigned the relative branching ratios of the photoproducts following excitation at 226 nm to the $\pi \rightarrow \pi^*$ state. They found that the major dissociation products were CH_3, NO_2, NO and O in order of decreased intensity under collision free con-

ditions. The production of NO is the first of a series of minor product pathways, where it can be formed following the absorption of a second photon by the NO_2 product in Eq. 1. The observation of CH_3NO by TOFMS in low branching ratio suggests and oxygen elimination pathway:

$$CH_3NO_2 \xrightarrow{h\nu} CH_3NO + O \tag{3.2}$$

Additionally, the authors observe the CH_3O fragment in collisional conditions suggesting the possibility of the *so-called* nitro-nitrite isomerization mechanism:

$$CH_3NO_2 \xrightarrow{h\nu} CH_3ONO \rightarrow CH_3O + NO. \tag{3.3}$$

This pathway was only observed under collisional conditions suggesting a concerted collision-free pathway would be non-existent, however, it has been observed thermally[71, 72] in the ground state as a competitive process with the C-N cleavage in the excited state.

Previous theoretical studies have focused primarily on ground state processes. Reaction paths and stationary point calculations have been carried out at the DFT/G2MP2[73] and UCCSD(T)/CBS[74] levels of theory. Dynamics on the ground state have mostly focused on roaming mediated isomerization to form the methyl nitrite isomer[75–77]. Previous excited state studies have focused on *ab initio* reaction path calculations using CASPT2[78–80] and most recently fewest-switches surface hopping (FSSH)/CIS[81] and *ab inito* multiple spawning (AIMS)/CASSCF[82] dynamics simulations. In both cases, the studies pertain to the dynamics of the weak 275 nm band corresponding to the $n \rightarrow \pi^*$ transition. To the best of our knowledge, there exist no excited state dynamics studies of nitromethane following absorption at 198 nm.

In order to properly elucidate the major and minor reaction pathways occurring in the ultrafast relaxation of nitromethane, *ab initio* molecular dynamics calculations were employed. The timescales for the de-excitation are calculated using on-the-fly *ab initio* multiple spawning (AIMS) simulations[15–17].

3.4 Computational Details

In the AIMS simulations, the adiabatic energies, gradients and non-adiabatic couplings required to evaluate the equations-of-motion (EOMs) were calculated at

the restricted active space self-consistent field (RASSCF)[7] level of theory. The separation of the occupied and virtual orbitals, consisted of the following active spaces. RAS1 contained the $2S_N$ (a′), σ_{NO} (a′), σ_{NO} (a″), and π_{NO} (a′). RAS2 contained the σ_{CN} (a′), nσ_O (a″), nπ_O (a″) and π^*_{NO} (a′) orbitals. RAS3 contained the σ_{NO} (a′), σ_{NO} (a″) and σ_{CN} (a′) orbitals. This level of theory is denoted RASSCF(2,4,2,3)/CAS(6,4), where the RASSCF contains at most two holes in RAS1 containing four occupied orbitals and at most two electrons in RAS3 containing three virtual orbitals. In the RASSCF calculations, state averaging was performed over the lowest four singlet states, corresponding to 1A′ (π^2_{NO}), 1A″ ($\pi^*_{NO} \leftarrow \sigma_{CN}$), 2A′ ($\pi^*_{NO} \leftarrow$ nσ_O), and 2A″ ($\pi^*_{NO} \leftarrow$ nπ_{NO}) at the Franck-Condon (FC) point. The small Atomic Natural Orbital basis, denoted ANO-S, was used in all calculations with the contractions C,N,O[4s3p1d],H[2s1p] employed. All electronic structure calculations were performed using the COLUMBUS[51] and MOLCAS[83] set of programs.

The use of RASSCF was essential to the correct optimization of the orbital energies and coefficients. Previously, it has been demonstrated that symmetry broken solutions of the wavefunction arise in the CASSCF optimization of the NO_2 radical (i.e. the doublet ground state of NO_2)[84]. This results if certain occupied or virtual orbitals are excluded from the active space. It was determined that a set of properly symmetrized orbitals are needed in the description of the excited electronic states of NO_2. The results of this paper required an active space consisting of 13 electrons in 11 orbitals for NO_2. The present work deals with the description of NO_2 in the excited state and it has been previously shown that this requirement applies to nitromethane[78, 80]. The solution to the large CAS space is to divide the subspace into RAS1, RAS2, and RAS3, whereby occupied and virtual orbitals that contribute marginally to the description of the electronic states are placed in RAS1 and RAS3 respectively. This choice of active space is shown in Fig. 3.2, where the orbitals 10-13, 14-17 and 18-20 are contained in RAS1, RAS2 and RAS3, respectively.

The initial position and momenta for the trajectories were sampled from a ground vibrational state Wigner distribution. A harmonic approximation is assumed, with the required normal modes and frequencies calculated at the coupled-cluster with single, double, and perturbative triple excitations [CCSD(T)]/aug-cc-pVDZ level of theory using the CFOUR program[52]. A total of 25 initial basis function were used for a propagation time of 100 fs. At the end of the AIMS simulation, a total of 78 basis functions had been spawned.

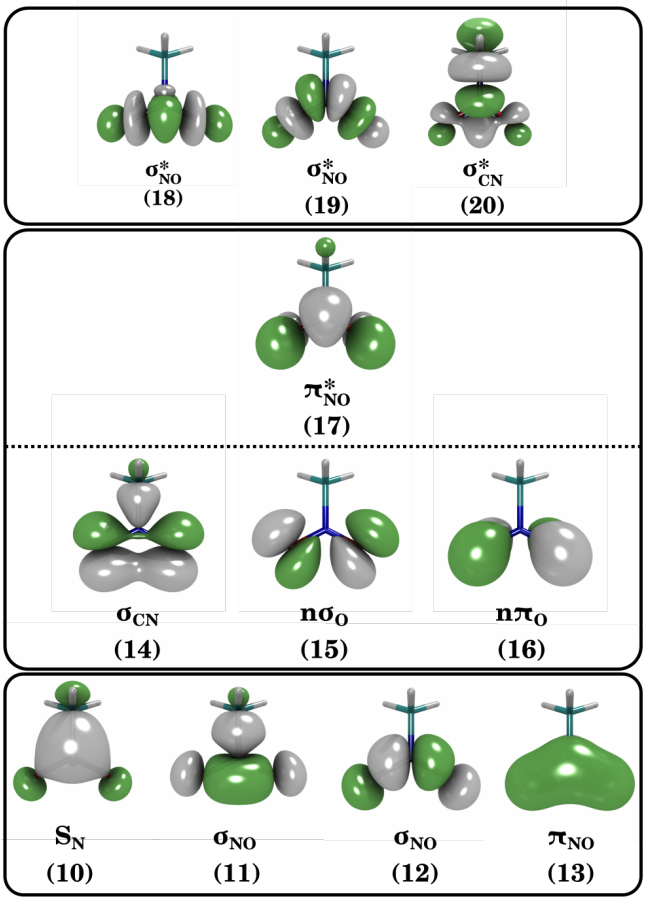

Figure 3.2: RASSCF orbitals optimized over the lowest three singlet states. Here the dashed horizontal line indicates the division between occupied and virtual orbitals.

3.5 Results

3.5.1 Potential Energy Surfaces

Table 3.1 lists the vertical excitation energies of the first three lowest singlet excited states. The calculated RASSCF energies used in the AIMS simulations are compared to previous high level CASPT2 results[78] at the FC point. The comparison shows that the states differ by ≈0.3 eV in S_1 and S_2, and by ≈1.0 eV in S_3. This arises from the lack of dynamical correlation in the RASSCF wavefunction which can be corrected by performing configuration interaction (CI) singles or doubles to give a RASCI description of the wavefunction. Presently, this adds an additional computational cost that makes this option impractical and therefore the RASSCF description of the wavefunction is used. It has been demonstrated in Appendix 5.2.2, that the curvature and barrier height of the electronic states along the C-N dissociation coordinate is reproduced with this level of theory, however, shifted vertically relative to benchmark calculations.

Table 3.1: Vertical excitation energies of nitromethane calculated at the Franck-Condon point.

State	Symmetry[a]	Character	DFT/MRCI aug-cc-pVDZ	CASPT2[b] ANO [4s3p2d/3s2p1d]	RASSCF[c] ANO [4s3p1d/2s1p]
S_1	1A″	σ(CN) $\longrightarrow$ π^*(NO)	3.89	4.07	4.26
S_2	2A′	n_O $\longrightarrow$ π^*(NO)	4.22	4.35	4.67
S_3	2A″	$n\pi_O$ $\longrightarrow$ π^*(NO)	6.18	6.36	7.35

[a] C_s minimum
[b] CASSCF(14e,11o)
[c] RASSCF(2,4,2,3)/CAS(6,4)

The first excited state (S_1) corresponds to excitation from the σ_{CN} orbital to the π^*_{NO} orbital localized on the NO_2 moeity. This state is not optically dark but has a vanishingly low oscillator strength ($f = 6.00\times10^{-6}$). S_2 is an optically dark state located ≈0.40 eV above S_1, corresponding to excitation from the nσ_O orbital to the π^*_{NO} orbital ($f = 2.40\times10^{-5}$). S_3 is an optically bright state ($f = 2.09\times10^{-1}$) corresponding to excitation from the nπ_O orbital to the π^*_{NO} at the absorption maximum of the 6.25 eV band. In order to understand the dynamics occurring on the

excited state, the potential energy surfaces for select nuclear degrees of freedom are considered. These correspond to the C-N bond dissociation coordinate, $\mathbf{r}_{\mathrm{CN}}$ and the N-O dissociation coordinate, $\mathbf{r}_{\mathrm{NO}}$.

Figure 3.3 shows the adiabatic potential energy surfaces (PESs) as a function of the $\mathbf{r}_{\mathrm{CN}}$ and $\mathbf{r}_{\mathrm{NO}}$ calculated at the RASSCF/ANO-S[4s3p1d/2s1p] level of theory. Figure 3.3(a) shows a steep barrier of ≈0.50 eV on the $2A''$ state that leads to the dissociation of nitromethane to form a methyl cation (CH_3) + NO_2. Here, there is a small discontinuity in the PES that corresponds to a weakly coupled avoided crossing to a $\pi\sigma^*$ state that changes the character of the lower state. Figure 3.3(b) shows the intersection formed between S_3 and S_2 as the N-O bond elongates by 0.2 Å. The $\mathbf{r}_{\mathrm{NO}}$ coordinate is the most energetically favourable, following photoexcitation at the absorption maximum of 6.25 eV.

3.5.2 Wavepacket Dynamics Simulation

The AIMS wave-packet propagation was performed starting on the S_3 optically bright state with 25 initial trajectory basis functions (TBFs) that spawn a total of 78 additional basis functions throughout the simulation. Shown in Figure 3.4 are the adiabatic state populations taken from the AIMS simulations. The dynamics shows a large transfer of population from S_3 to S_2 within ∼40 fs, with S_2 immediately transferring population to the lowest electronic states S_1 and S_0.

To better understand the RASSCF dynamics, one-dimensional reduced nuclear densities calculated from the AIMS simulations are shown in Fig. 3.5. In Fig. 3.5(a), the calculated reduced densities for the C-N stretching coordinate are shown as a function of time. It is shown that large C-N stretching occurs on the excited state with in the first 40 fs. The component of the wavepacket that corresponds to the elongation of the C-N bond, has a revival by 60 fs before the simulations have completed. Fig. 3.5(b) shows the calculated reduced densities for the N-O stretching coordinate. Here, the wavepacket experiences a minor bifurcation of the wavepacket after 20 fs, leading to the dissociation of an oxygen atom and a revival of the wavepacket to the FC region. Fig. 3.5(c) shows the calculated reduced densities for the C-O distance as a function of time. It is shown that the distance between the two atoms has a periodic decrease in distance that returns to the FC region within 60 fs.

3.6 Discussion

3.6.1 Electronic Structure Calibration

The optimization of the orbitals and coefficients by RASSCF allowed for efficient calculation of the PESs for use in the AIMS simulation. The importance of the RASSCF calculations was twofold: (i) it resulted in reducing the computational cost in the state-averaged optimization of the orbitals and coefficients, and (ii) the relative barrier heights on the excited states for the dissociative processes were comparable to benchmark calculations. A detailed analysis of the choice of active space is described below.

The present study employed a RASSCF(2,4,2,3)/CAS(6,4) space to generate the same orbitals of a full valence CAS(14,11) calculation but at a reduced computational cost. At the CASSCF level of theory, this large active space is far too computationally costly for *on-the-fly* dynamics simulations and has been noted as the reason for why no previous dynamics studies exist following excitation to the absorption maximum at 6.25 eV[78–80]. Approximations, such as the truncation of the active space have been tested, however, this leads to pathological discontinuities along the PESs in regions where states cross and where the character of the states change. For instance, by truncating the CAS(14,11) active space by excluding one virtual orbital to CAS(14,10), the computational time is significantly reduced. The exclusion of one virtual orbital, results in the CASSCF wavefunction making a choice between including the σ^*_{CN} orbital or including the additional σ^*_{NO} orbital.

In Fig. 3.6, the potential energy cuts along the $\mathbf{r}_{\mathrm{CN}}$ coordinate are shown. The PESs in Fig. 3.6(a) were calculated by including the σ^*_{CN} orbital, which results in surfaces that accurately describe the molecule in the dissociation asymptote. In Fig. 3.6(b) the PESs were computed using an active space that excluded the σ^*_{CN} orbital and included the σ^*_{NO} orbital, which results in the poor description of the potential energy surfaces along the $\mathbf{r}_{\mathrm{CN}}$ coordinate. A detailed analysis of the AIMS dynamics using the CAS(14,10) active space is found in Appendix 5.2. Here, the initially sampled geometries exclude the σ^*_{CN} orbital, instead optimizing to the energetically favourable set of orbitals that include the σ^*_{NO} orbital. In the analysis performed in Appendix 5.2 it was demonstrated that the exclusion of one or more orbitals was shown to provide insufficient descriptions of the C-N dissociation coordinate which has been observed experimentally as the major photodissociation

channel. The bias imposed on the dynamics is one in which the wavepacket becomes trapped on S_2, transferring negligible population to S_1 and S_0. This trapping of the wavepacket on S_2 is the result of the exclusion of the σ^*_{CN} orbital and inclusion of the σ^*_{NO} orbital. As shown in Fig. 3.6(b), the major pathway involving cleavage of the C-N bond becomes energetically inaccessible with results in only the minor oxygen loss pathway being described. It is noted that on the basis of the CASSCF and RASSCF results that the electronic structure calibration is essential in describing the PESs that inform the dynamics simulations.

3.6.2 Quantum Dynamics

The AIMS simulations show that the dynamics that follow excitation to the absorption maximum at 6.25 eV, corresponds to the major pathway (Eq. 3.1) involving the cleavage of the C-N bond, and the minor pathway (Eq. 3.2) involving the oxygen loss pathway. The initially prepared excited state (S_3) shows rapid population transfer to S_2 within 20 fs that corresponds to the elongation of the N-O bond. This is shown in Fig. 3.5(b), where the wavepacket begins to bifurcate with one component of the wavepacket returning to the N-O equilibrium bond length and the other component corresponding to increased bond lengths. This increase in bond lengths corresponds to the accumulation of population on S_2 from S_3 as shown in Fig. 3.4. Within 40 fs, S_1 population begins to accumulate and corresponds to equilibrium bond lengths in the reduced density calculations in Fig. 3.5. This suggests that the components of the wavepacket on this state correspond to bound nitromethane.

The dynamics on S_1 show largely bound nitromethane which is consistent with the short bond lengths shown in Fig. 3.5 the calculation of the reduced nuclear densities. The rise in population on S_0 at 60 fs corresponds to nuclear geometries characterized by longer C-N bonds. This can be seen in Fig. 3.5(a), where at 60 fs the C-N bond lengths are elongated relative to the N-O and C-O bond lengths, suggesting the C-N bond is cleaving on that state. The reduced nuclear densities do not suggest that the isomerization mechanism occurs, corresponding to the formation of methyl nitrite (CH_3ONO). This is demonstrated by C-O bond lengths that increase, rather than decrease below the equilibrium bond length as a function of time as shown in Fig. 3.5(c).

3.7 Conclusion

The challenging problems in describing the electronic structures of nitromethane along the various major and minor reaction pathways have been investigated with the restricted active-space self-consistent field (RASSCF) method. The results show that the RASSCF calculations are ideal for the description of the lowest excited states in nitromethane, where a previously large CASSCF active space was computationally impractical for use in an *on-the-fly* dynamics study. The current study finds that the dynamics following excitation to the absorption maximum at 6.25 eV, correspond to rapid population transfer from the initial bright state (S_3) to the lower excited states. The dynamics on the excited state are characterized by vibrational motions corresponding to the C-N and N-O stretching coordinates that promote dissociation on the excited and ground states. The results confirm the major pathway corresponding to direct cleavage of the C-N bond: $CH_3NO_2 \xrightarrow{h\nu} CH_3 + NO_2$. Additionally, the results suggest the minor (i) direct oxygen loss: $CH_3NO_2 \xrightarrow{h\nu} CH_3NO + O$ occurs, while the (ii) nitro-nitrite isomerization: $CH_3NO_2 \xrightarrow{h\nu} CH_3ONO$ pathway does not occur.

3.8 Future Work

The initial RASSCF dynamics results have shown generally good agreement with previous studies of nitromethane. Future work will focus on the simulation of the dynamics by including dynamic correlation effects from multireference first-order configuration interaction (MR-FOCI) calculations. This will provide additional confidence in the results and allow for the direct comparison of a calculated TRPES to previously published results[85]. Additionally, nitromethane possesses three first row elements that are of interest in light of recent development of time-resolved X-ray spectroscopy laser systems. The results of the dynamics can be further validated by calculation X-ray absorption and photoelectron spectra that are sensitive to the local environment surrounding each atom.

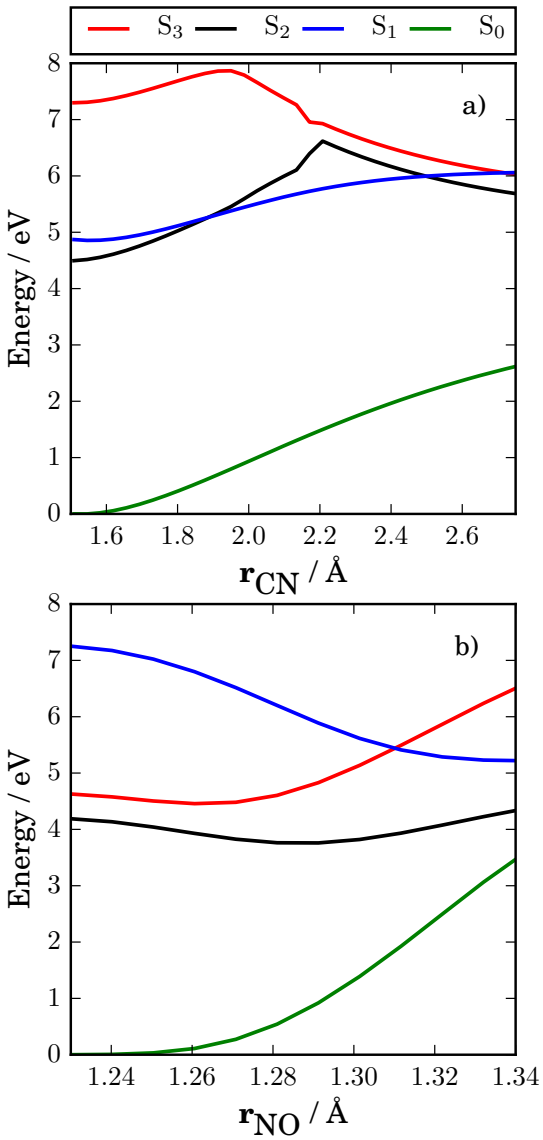

Figure 3.3: Potential energy surface cuts along the C-N (a) and N-O (b) bond dissociation internal coordinates calculated at the RASSCF ANO-S C,N,O[4s3p1d]/H[2s1p] level of theory.

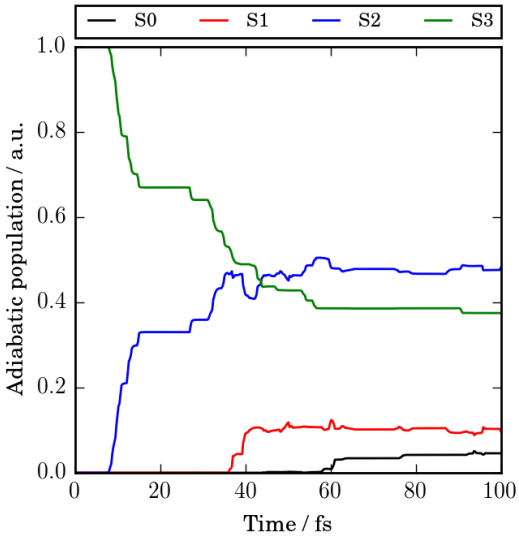

Figure 3.4: The time-evolution of the adiabatic state populations taken from the AIMS simulations.

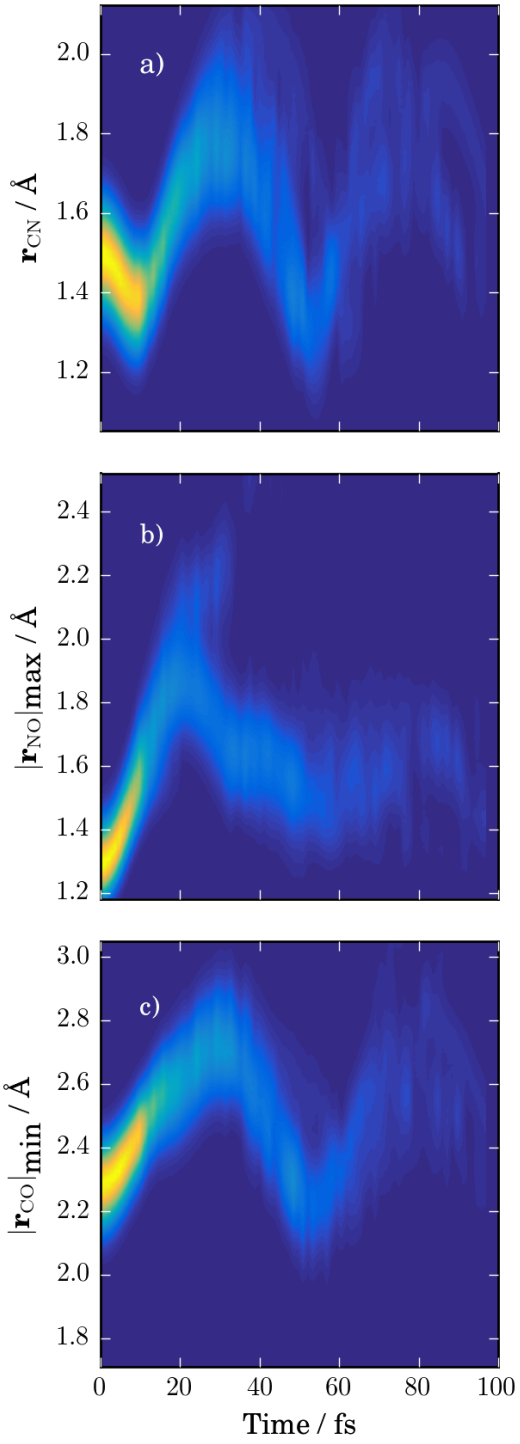

Figure 3.5: One dimensional reduced nuclear densities calculated from the AIMS simulations. (a) the C-N stretch coordinate, (b) The maximum N-O stretch coordinate, (c) and the minimum C-O distance.

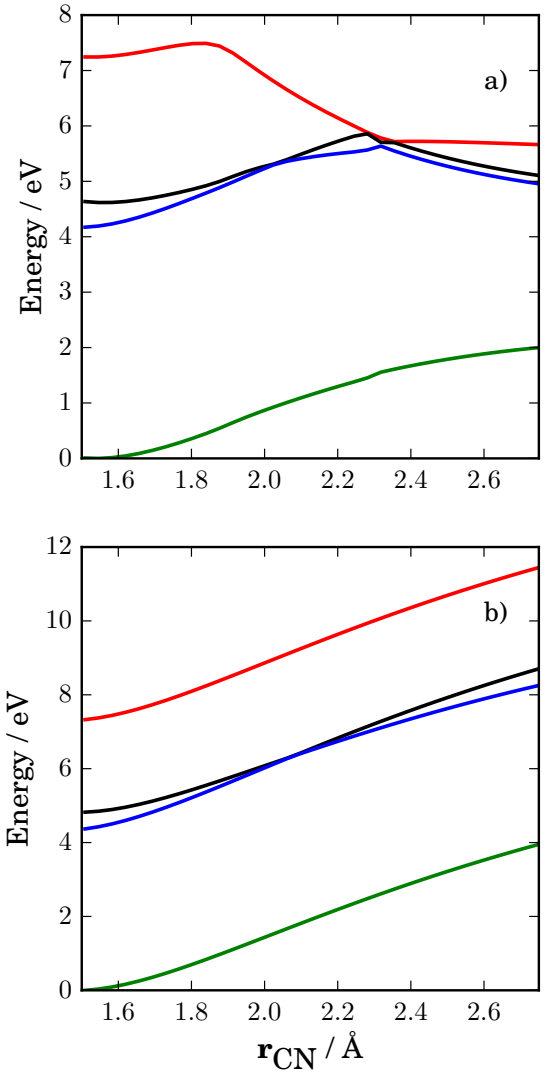

Figure 3.6: Potential energy surface cuts along the C-N bond dissociation coordinates calculated at the CAS(14,10) ANO-S C,N,O[4s3p1d]/H[2s1p] level of theory. The surfaces (a) with and (b) without the inclusion of the σ^*_{CN} orbital in the active space.

Chapter 4

Conclusion

In the work that has been presented, two molecular systems have been studied. The studies in both cases involved complex electronic structuere that required attention in order to describe the dynamics that occurs prior to bond-breaking and bond-formation. In the two systems studied, significant work was completed in order to understand the necessary electronic structures that were needed to describe the initial conditions of the systems.

In Chapter 2, cyclopropane was investigated in a joint theoretical/experimental study by time-resolved photoelectron spectroscopy (TRPES) and *ab initio* dynamics simulations. Despite the extensive literature on cyclopropane, no previous studies focused on the time-resolved dynamics both theoretically and experimentally. Preceding the present study, it was shown that previous interpretations of the experimental VUV absorption spectrum were incorrect in describing the Jahn-Teller (JT) split states that arose from JT active normal mode vibrations. Through an *ab initio* simulation using the multiconfigurational time-dependent Hartree (MCTDH) wavepacket propagation method, the initially prepared states following photoexcitation at 160.8 nm were re-interpreted. The results showed that four initially prepared excited states became split by JT distortions into nine electronic states, where the relative populations became split over the lowest four split electronic states with the following populations: S_1 (33%), S_2 (12%), S_3 (30%) and S_4 (25%). The results of this previous work were integral in the interpretation of the TRPES spectrum by *ab initio* dynamics simulations. Using the initial populations from the re-interpretation of the pump pulse, the dynamics were investigated for the four lowest electronically excited states. The simulations were performed using the *ab initio* multiple spawning (AIMS) algorithm informed by multireference configuration interaction (MRCI)

electronic structure calculations.

The dynamics that followed excitation at 160.8 nm were defined by a rapid ring opening and dissociation of cyclopropane to form ethylene and methylene. The initially prepared wavepacket was split over the two higher lying states S_3 and S_4 and two lower lying states S_1 and S_2. The dynamics on the lower lying states were characterized by prompt dissociation, while the higher lying states showed that the molecule experiences ring-opening and non-radiative decay to S_1 and S_2 before undergoing dissociation on those states. The result is that the components of the wavepackets on the different states can be uniquely assigned to regions of the TRPES spectrum. The dynamics initiated on the higher lying states give rise to the observed signal at 1.9 eV and correspond to the entirely ring closed species. The component of the wavepacket on the lower lying states gives rise to the observed signal at 1.3 eV and corresponds to a molecular species that is ring-opened and dissociated on that state.

In Chapter 3, nitromethane was studied by electronic structure theory and *ab initio* dynamics simulations. The spectroscopy of nitromethane has been well studied experimentally and theoretically, particularly the dissociation and isomerization pathways. The present study focused on the necessary electronic structure calculations that enabled a dynamics study. The computational requirements in the description of the major and minor reaction coordinates, permitted a large active space to be selected. The restricted active-space self-consistent field (RASSCF) method was employed to extend a smaller active space by including orbitals necessary to the description of the wavefunction. Using the RASSCF description of the three lowest electronically excited states, the dynamics were investigated using the *ab initio* multiple spawning (AIMS) algorithm. The dynamics that followed excitation to the absorption maximum centered at 6.25 eV, corresponded to rapid population transfer to the lowest excited states. This was mediated by the elongation of the N-O bond at the intersection between S_3 and S_2. The molecular dynamics on the lowest excited states showed C-N bond dissociation, in general agreement with the major reaction pathway.

In both studies, a mechanistic picture was assigned to the dynamics that occurred on the excited state. This required a robust method of electronic structure theory capable of describing the molecules around and beyond equilibrium. The excited state dynamics simulations performed using the AIMS algorithm have enabled the relative timescales for the photo-decay to be assigned. In cyclopropane, the question

of how the reactants become the products was definitively stated and mapped to an experimental observable. In nitromethane, the electronic structure was shown to be necessary in the correct determination of the excited state PESs that would enable a dynamics study.

Chapter 5

Appendix

5.1 Cylcopropane

The D_{3h} S_0 optimized geometry for C_3H_6 used in all electronic structure calculations:

C	0.000000	0.000000	0.871758
C	-0.754964	0.000000	-0.435879
C	0.754964	0.000000	-0.435879
H	0.000000	0.911300	1.453890
H	0.000000	-0.911300	1.453890
H	-1.259106	0.911300	-0.726945
H	-1.259106	-0.911300	-0.726945
H	1.259106	0.911300	-0.726945
H	1.259106	-0.911300	-0.726945

5.2 Nitromethane

The C_s S_0 optimized geometry for CH_3NO_2 used in all electronic structure calculations:

C	-0.00238920	1.40686859	0.00000000
N	-0.00052595	-0.09519309	0.00000000
O	0.00016276	-0.65040109	-1.09653804
O	0.00016276	-0.65040109	1.09653804
H	1.05094267	1.73193488	0.00000000
H	-0.51017671	1.74202128	-0.91521594
H	-0.51017671	1.74202128	0.91521594

5.2.1 Details of Quantum Dynamics Simulation

The AIMS wave-packet propagation was performed 25 initial trajectory basis functions (TBFs) on the optically bright S_3 state, that resulted in a total of 100 additional basis functions spawned during the simulation. Shown in Figure 5.1 are the adiabatic state populations taken from the AIMS simulations. Here, it can be seen that the initially prepared state (S_3) decays to S_2 within ~20 fs, followed by a slow increase in the S_1 population.

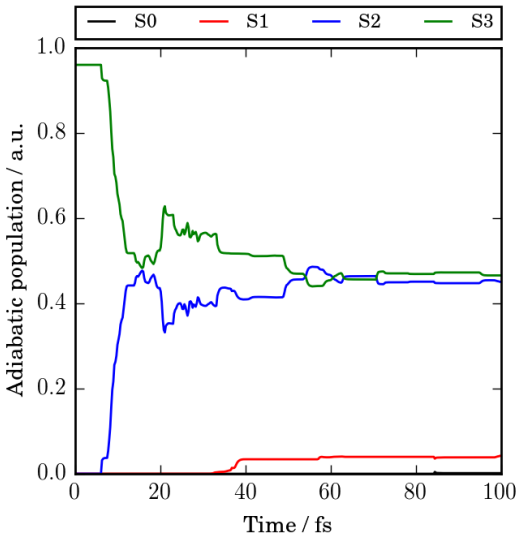

Figure 5.1: The time-evolution of the adiabatic state populations taken from the AIMS simulations.

In order, to understand the dynamics that lead to the observed adiabatic state populations, one-dimensional reduced nuclear densities calculated from the AIMS simulations are shown. Fig. 5.2(a) shows the nuclear densities for the $\mathbf{r}_{CN}$ coordinate coordinate. Here it can be seen that the initially prepared wavepacket, oscillates around the equilibrium bond length with a period consistent with C-N bond

stretching. This oscillation coincides with the transfer of population between S_3 and S_2. Fig. 5.2(b) shows the nuclear densities for the $\mathbf{r}_{NO}$ coordinate coordinate, where it is shown that the N-O bond immediately elongates by >1Å, leading to population transfer between S_3 and S_2 that is coupled to the C-N stretching motion. The wavepacket bifurcates with a large portion of the density showing the loss of an Oxygen. The results of this show that there is a bias with the choice of active space, whereby, the exclusion of the σ^*_{CN} orbital results in the Oxygen loss pathway being the dominant pathway, despite previous literature suggesting it to be a minor channel. It is determined that the correct description of the wavefunction must consist of a wavefunction with an active space of 14 electrons in 11 orbitals. The results of this treatment of the dynamics are described in Chapter 3.5.2.

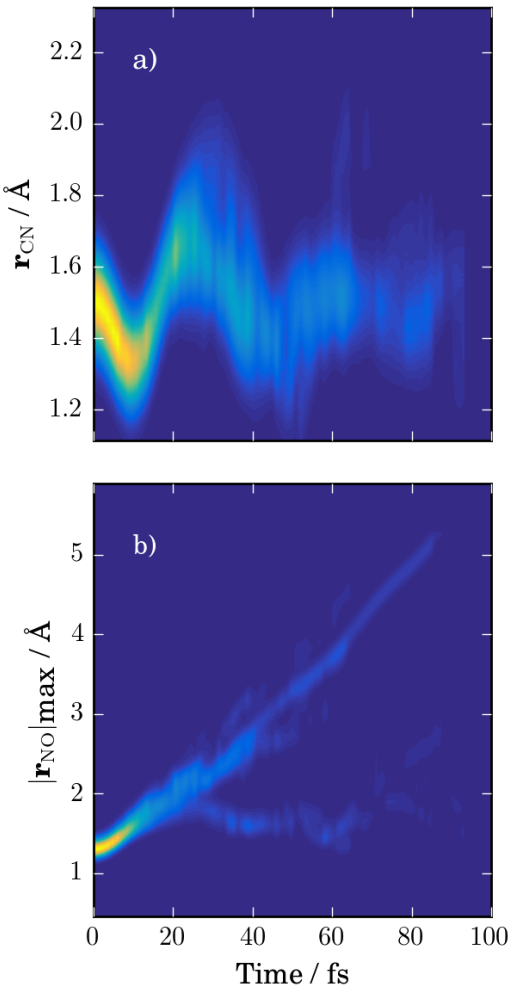

Figure 5.2: One dimensional reduced nuclear densities calculated from the AIMS simulations. (a) the C-N stretch coordinate. (b) The N-O stretch coordinate.

5.2.2 Potential Energy Surface Characterization

Fig. 5.3 shows the potential energy surfaces along the C-N dissociation coordinate for the four lowest electronic states. It can be noted that the relative barrier height is approximated well by the RASSCF calculations, with the energy being shifted by 0.45 eV. It is also noted that the onset of the barrier is closer for the RASSCF potential energy surfaces by 0.1 Å, which is the result of less electron correlation being included in the wavefunction by permitting only double excitations into RAS3.

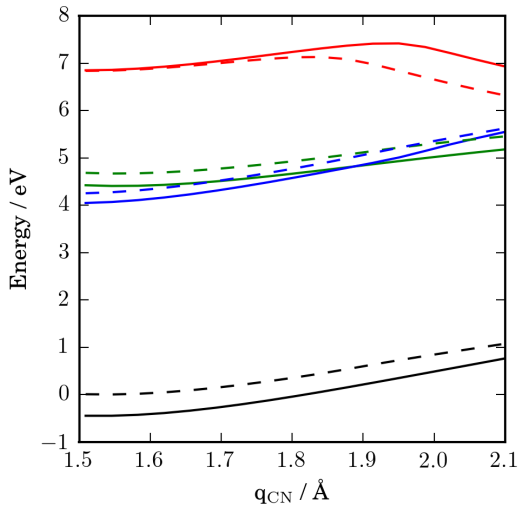

Figure 5.3: The barrier and curvature of the C-N dissociation coordinate calculated at the (i) CAS(14,11)/MR-FOCI 6-31+G* and (ii) RASSCF(2,4,2,3)/CAS(6,4) ANO-S C,N,O[4s3p1d],H[2s1p] levels of theory. The comparison is shown with an energy shift of -0.45 eV applied to the RASSCF potential energy surfaces.

Bibliography

[1]M. Born and K. Huang, *Dynamical theory of crystal lattices* (Clarendon, 2002).

[2]M. Born and R. Oppenheimer, Ann. Phys. **389**, 457–484 (1927).

[3]W. Pauli, Z. Phys. **31**, 765–783 (1925).

[4]A. Szabo and N. S. Ostlund, *Modern quantum chemistry: introduction to advanced electronic structure theory* (Dover Publications, Inc., 1996).

[5]D. R. Hartree, Math. Proc. Camb. Philos. Soc. **24**, 111–132 (1928).

[6]B. O. Roos, "The complete active space self-consistent field method and its applications in electronic structure calculations", in *Advances in chemical physics* (John Wiley & Sons, Ltd, 2007), pp. 399–445.

[7]P. Å. Malmqvist, A. Rendell, and B. O. Roos, J. Phys. Chem. **94**, 5477–5482 (1990).

[8]J. C. Tully, J. Chem. Phys. **93**, 1061–1071 (1990).

[9]F. A. Bornemann, P. Nettesheim, and C. Schütte, J. Chem. Phys. **105**, 1074–1083 (1996).

[10]J. E. Subotnik, A. Jain, B. Landry, A. Petit, W. Ouyang, and N. Bellonzi, Annual Review of Physical Chemistry **67**, 387–417 (2016).

[11]H. Meyer and W. H. Miller, J. Chem. Phys. **70**, 3214–3223 (1979).

[12]X. Li, J. C. Tully, H. B. Schlegel, and M. J. Frisch, J. Chem. Phys. **123**, 084106 (2005).

[13]E. J. Heller, J. Chem. Phys. **62**, 1544–1555 (1975).

[14]E. J. Heller, J. Chem. Phys. **75**, 2923–2931 (1981).

[15]T. J. Martínez, M. Ben-Nun, and R. D. Levine, J. Phys. Chem. **100**, 7884 (1996).

[16]T. J. Martínez, M. Ben-Nun, and R. D. Levine, J. Phys. Chem. A **101**, 6389 (1997).

[17]M. Ben-Nun, J. Quenneville, and T. J. Martínez, J. Phys. Chem. A **104**, 5161 (2000).

[18]R. Berera, R. van Grondelle, and J. T. M. Kennis, Photosynth. Res. **101**, 105–118 (2009).

[19]A. Stolow, A. E. Bragg, and D. M. Neumark, Chem. Rev. **104**, 1719–1758 (2004).

[20]W. Domcke, D. R. Yarkony, and H. Köppel, *Conical intersections* (World Scientific Publishing, 2011), pp. 663–667.

[21]M. Spanner, S. Patchkovskii, C. Zhou, S. Matsika, M. Kotur, and T. C. Weinacht, Phys. Rev. A **86**, 053406 (2012).

[22]H. N. C. Wong, M. Y. Hon, C. W. Tse, Y. C. Yip, J. Tanko, and T. Hudlicky, Chem. Rev. **89**, 165 (1989).

[23]K. Mizuno, N. Ichinose, and Y. Yoshimi, J. Photochem. Photobiol., C **1**, 167 (2000).

[24]N. Hoffmann, Chem. Rev. **108**, 1052 (2008).

[25]R. Srinivasan and J. A. Ors, J. Org. Chem. **44**, 3426 (1979).

[26]R. Srinivasan, T. Baum, and J. A. Ors, Tetrahedron Lett. **22**, 4795 (1981).

[27]T. Baum, A. Rossi, and R. Srinivasan, J. Am. Chem. Soc. **107**, 4411 (1985).

[28]W. J. Leigh and R. Srinivasan, Acc. Chem. Res. **20**, 107 (1987).

[29]W. Duch and G. A. Segal, J. Chem. Phys. **79**, 2951 (1983).

[30]W. Duch and G. A. Segal, J. Chem. Phys. **84**, 544 (1986).

[31]J. W. Zwanziger, A. Ghelichkhani, and E. R. Grant, J. Chem. Phys **89**, 4012 (1988).

[32]C. Rowland, Chem. Phys. Lett. **9**, 169 (1971).

[33]K. Krogh-Jespersen and H. D. Roth, J. Am. Chem. Soc. **114**, 8388 (1992).

[34]D. J. Mann and W. L. Hase, J. Am. Chem. Soc. **124**, 3208 (2002).

[35]Z. Li, X. Chen, X. Shan, T. Liu, and K. Xu, J. Chem. Phys. **130**, 054302 (2009).

[36]C. L. Currie, H. Okabe, and J. R. McNesby, J. Phys. Chem. **67**, 1494 (1963).

[37]A. A. Scala and P. Ausloos, J. Chem. Phys. **49**, 2282 (1968).

[38]S. Kazuhiko, O. Kin-ichi, and I. Tanaka, Bull. Chem. Soc. Jpn. **48**, 1974 (1975).

[39]C. C. Wang, Y. T. Lee, J. J. Lin, J. Shu, Y.-Y. Lee, and X. Yang, J. Chem. Phys. **117**, 153 (2002).

[40]M. B. Robin and N. A. Kuebler, J. Chem. Phys **69**, 806 (1978).

[41]P. Wagner and A. B. F. Duncan, J. Chem. Phys **21**, 516 (1953).

[42]M. Gingell, N. J. Mason, I. C. Walker, G. Marston, H. Zhao, and M. R. F. Siggel, J. Phys. B: At., Mol. Opt. Phys. **32**, 2729 (1999).

[43]I. C. Walker, D. M. P. Holland, D. A. Shaw, I. J. McEwen, and M. F. Guest, J. Phys. B **40**, 1875 (2007).

[44]S. P. Neville, A. Stolow, and M. S. Schuurman, **149**, 144310 (2018).

[45]R. Forbes, V. Makhija, K. Véyrinas, A. Stolow, J. W. L. Lee, M. Burt, M. Brouard, C. Vallance, I. Wilkinson, R. Lausten, and P. Hockett, J. Chem. Phys. **147**, 013911 (2017).

[46]M. Ghotbi, M. Beutler, and F. Noack, Opt. Lett. **35**, 3492 (2010).

[47]A. T. J. B. Eppink and D. H. Parker, Rev. Sci. Instrum. **68**, 3477–3484 (1997).

[48]Y. T. Cho and S.-J. Na, Meas. Sci. Technol. **16**, 878 (2005).

[49]M. Ben-Nun and T. J. Martínez, Adv. Chem. Phys. **121**, 439 (2002).

[50]B. T. Pickup, Chem. Phys. **19**, 193 (1977).

[51]H. Lischka, R. Shepard, I. Shavitt, R. M. Pitzer, M. Dallos, T. Müller, P. G. Szalay, F. B. Brown, R. Ahlrichs, H. J. Böhm, A. Chang, D. C. Comeau, R. Gdanitz, H. Dachsel, C. Ehrhardt, M. Ernzerhof, P. Höchtl, S. Irle, G. Kedziora, T. Kovar, V. Parasuk, M. J. M. Pepper, P. Scharf, H. Schiffer, M. Schindler, M. Schüler, M. Seth, E. A. Stahlberg, J.-G. Zhao, S. Yabushita, Z. Zhang, M. Barbatti, S. Matsika, M. Schuurmann, D. R. Yarkony, S. R. Brozell, E. V. Beck, J.-P. Blaudeau, M. Ruckenbauer, B. Sellner, F. Plasser, J. J. Szymczak, R. F. K. Spada, and A. Das., see https://www.univie.ac.at/columbus/ (2017).

[52]J. F. Stanton, J. Gauss, M. E. Harding, P. G. Szalay, A. A. Auer, R. J. Bartlett, U. Benedikt, C. Berger, D. E. Bernholdt, Y. J. Bomble, L. Cheng, O. Christiansen, M. Heckert, O. Heun, C. Huber, T. C. Jagau, D. Jonsson, J. Jusélius, K. Klein, W. J. Lauderdale, D. A. Matthews, T. Metzroth, L. A. Mück, D. P. O'Neill, D. R. Price, E. Prochnow, C. Puzzarini, K. Ruud, F. Schiffmann, W. Schwalbach, C. Simmons, S. Stopkowicz, A. Tajti, J. Vázquez, F. Wang, and J. D. Watts, *Cfour,*

coupled-cluster techniques for computational chemistry, a quantum-chemical program package, see http://www.cfour.de.

[53]D. Holland, L. Karlsson, and K. Siegbahn, J. Electron Spectrosc. **125**, 57 (2002).

[54]H. Basch, M. B. Robin, N. A. Kuebler, C. Baker, and D. W. Turner, J. Chem. Phys. **51**, 52 (1969).

[55]F. Leng and G. Nyberg, J. Electron. Spectrosc. Relat. Phenom. **11**, 293 (1977).

[56]P. Keller, J. Taylor, T. A. Carlson, T. Whitley, and F. Grimm, Chem. Phys. **99**, 317 (1985).

[57]S.-H. Lee, K.-C. Tang, I.-C. Chen, M. Schmitt, J. P. Shaffer, T. Schultz, J. G. Underwood, M. Z. Zgierski, and A. Stolow, J. Phys. Chem. A. **106**, 8979–8991 (2002).

[58]O. Schalk, A. E. Boguslavskiy, and A. Stolow, J. Phys. Chem. A. **114**, 4058–4064 (2010).

[59]L. S. Cederbaum, H. Köppel, and W. Domcke, Int. J. Quantum Chem. **15**, 251 (1981).

[60]H. Köppel, W. Domcke, and L. S. Cederbaum, Adv. Chem. Phys. **57**, 59 (1984).

[61]H. Köppel, W. Domcke, and L. S. Cederbaum, "Conical intersections: electronic structure, dynamics & spectroscopy", in, Vol. 15 (World Scientific Publishing, 2004) Chap. 7, p. 323.

[62]M. H. Beck, A. Jäckle, G. A. Worth, and H.-D. Meyer, Phys. Rep. **324**, 1 (2000).

[63]J. D. Coe and T. J. Martinez, Molecular Physics **106**, 537–545 (2008).

[64]G. Herzberg, Can. J. Phys. **39**, 1511 (1961).

[65]B. A. Williams and T. A. Cool, J. Chem. Phys. **94**, 6358 (1991).

[66]I. C. Walker and M. A. Fluendy, Int. J. Mass Spectrom. **205**, 171–182 (2001).

[67]S. Nagakura, Molecular Physics **3**, 152–162 (1960).

[68]N. S. Bayliss and E. G. McRae, J. Phys. Chem. **58**, 1006–1011 (1954).

[69]W. D. Taylor, T. D. Allston, M. J. Moscato, G. B. Fazekas, R. Kozlowski, and G. A. Takacs, Int. J. Chem. Kinet. **12**, 231–240 (1980).

[70]Y. Q. Guo, A. Bhattacharya, and E. R. Bernstein, J. Phys. Chem. A. **113**, 85–96 (2009).

[71]A. M. Wodtke, E. J. Hintsa, and Y. T. Lee, J. Phys. Chem. **90**, 3549–3558 (1986).

[72]A. M. Wodtke, E. J. Hintsa, and Y. T. Lee, J. Chem. Phys. **84**, 1044–1045 (1986).

[73]W.-F. Hu, T.-J. He, D.-M. Chen, and F.-C. Liu, J. Phys. Chem. A. **106**, 7294–7303 (2002).

[74]R. Zhu and M. Lin, Chem. Phys. Lett. **478**, 11–16 (2009).

[75]Z. Homayoon and J. M. Bowman, J. Phys. Chem. A. **117**, 11665–11672 (2013).

[76]R. S. Zhu, P. Raghunath, and M. C. Lin, J. Phys. Chem. A. **117**, 7308–7313 (2013).

[77]A. Dey, R. Fernando, C. Abeysekera, Z. Homayoon, J. M. Bowman, and A. G. Suits, J. Chem. Phys. **140**, 054305 (2014).

[78]J. F. Arenas, J. C. Otero, D. Peláez, and J. Soto, J. Chem. Phys. **119**, 7814–7823 (2003).

[79]J. F. Arenas, J. C. Otero, D. Peláez, and J. Soto, J. Chem. Phys. **122**, 084324 (2005).

[80]M. Isegawa, F. Liu, S. Maeda, and K. Morokuma, J. Chem. Phys. **140**, 244310 (2014).

[81]T. Nelson, J. Bjorgaard, M. Greenfield, C. Bolme, K. Brown, S. McGrane, R. J. Scharff, and S. Tretiak, J. Phys. Chem. A. **120**, 519–526 (2016).

[82]J. Ghosh, H. Gajapathy, A. Konar, G. M. Narasimhaiah, and A. Bhattacharya, J. Chem. Phys. **147**, 204302 (2017).

[83]F. Aquilante, J. Autschbach, R. K. Carlson, L. F. Chibotaru, M. G. Delcey, L. D. Vico, I. F. Galván, N. Ferré, L. M. Frutos, L. Gagliardi, M. Garavelli, A. Giussani, C. E. Hoyer, G. L. Manni, H. Lischka, D. Ma, P. Å. Malmqvist, T. Müller, A. Nenov, M. Olivucci, T. B. Pedersen, D. Peng, F. Plasser, B. Pritchard, M. Reiher, I. Rivalta, I. Schapiro, J. Segarra-Martí, M. Stenrup, D. G. Truhlar, L. Ungur, A. Valentini, S. Vancoillie, V. Veryazov, V. P. Vysotskiy, O. Weingart, F. Zapata, and R. Lindh, J. Comp. Chem. **37**, 506–541 (2016).

[84]C. P. Blahous, B. F. Yates, Y. Xie, and H. F. Schaefer, J. Chem. Phys. **93**, 8105–8109 (1990).

[85]S. Adachi, H. Kohguchi, and T. Suzuki, J. Phys. Chem. Letters **9**, 270–273 (2018).